

THE STRUCTURE OF RAPIDLY ROTATING LATE-TYPE SPIRALS: I. PHOTOMETRY, H I AND OPTICAL KINEMATICS

KRISTINE SPEKKENS¹ & RICCARDO GIOVANELLI²

Center for Radiophysics and Space Research, Cornell University, Ithaca, NY 14853

To appear in the Astronomical Journal

ABSTRACT

We present *I*-band photometry, long-slit optical spectroscopy, and new aperture synthesis H I observations for 8 late-type spirals with rotation velocities in the range $243 \text{ km s}^{-1} \lesssim V_{\text{rot}} \lesssim 308 \text{ km s}^{-1}$. The sample will be used to study the structure and angular momentum of disks at the high-mass end of the spiral galaxy population; here we discuss the basic properties of these “fast rotators”, and derive hybrid optical/H I rotation curves for each. Despite the presence of H I warps and low-mass companions in many systems, their kinematics are regular and there is excellent agreement between optical and H I tracers near the optical radius r_{opt} . At high inclinations where projection effects are negligible, the sample galaxies exhibit flat, featureless rotation curves out to their last measured points at $1.7 - 3.5 r_{\text{opt}}$. The intermediate inclination systems are also consistent with a constant rotation amplitude for $r \gtrsim 0.5 r_{\text{opt}}$. We therefore find no evidence for declining rotation curves at the high-mass end of the late-type spiral galaxy population. Combining our data with the compilation of spirals with reliable outer H I kinematics from Casertano & van Gorkom (1991), we find no convincing trends between logarithmic outer rotation curve slopes and rotation amplitudes or surface brightnesses for galaxies with $V_{\text{rot}} \gtrsim 220 \text{ km s}^{-1}$, and correlations with morphological types and disk scale-lengths in this regime are marginal.

Subject headings: galaxies: spiral — galaxies: kinematics and dynamics — galaxies: fundamental parameters

1. INTRODUCTION

The dynamics of rapidly rotating spirals provide insight into the structure of systems at the high-mass extreme of the galaxy population. Their properties are essential for understanding well-established trends between the rotation velocity V_{rot} of a disk galaxy and its other basic parameters, such as morphology, luminosity, surface brightness and baryon fraction. Observations of massive nearby galaxies also constitute a benchmark for studies of more distant systems, since the most luminous counterparts to local spirals are more easily detected at high redshift. “Fast rotators” in the local Universe thus hold important clues to the formation and evolution of the spiral galaxy population as a whole.

However, most recent studies of the kinematics of disk galaxies have focused on low mass and/or low surface brightness late-type systems (e.g. de Blok et al. 1996; de Blok & McGaugh 1997; Swaters 1999; Swaters et al. 2000; McGaugh et al. 2001; Marchesini et al. 2002; van den Bosch & Swaters 2001; van den Bosch et al. 2001; de Blok et al. 2001, 2003; Swaters et al. 2003; Rhee et al. 2004; Gentile et al. 2005; Simon et al. 2005; Spekkens et al. 2005; Valenzuela et al. 2005), while others have examined intermediate-mass systems (e.g. García-Ruiz et al. 2002; Kregel & van der Kruit 2004a; Kregel et al. 2005; Gentile et al. 2004, hereafter G04).

Observations of early type disk galaxies that span a wide range of morphological types and luminosities are now underway (Noordermeer et al. 2005), but high-quality, homogeneously processed data for late-type massive galaxies has so far been lacking. To fill this gap we present photometry and kinematics for 8 of these systems, which will be used to model the dark and luminous contributions to their mass profiles in a forthcoming paper (Spekkens & Giovanelli 2006, in preparation).

It has long been recognized that both the shapes and amplitudes of spiral galaxy rotation curves (RCs) change systematically with luminosity (e.g. Roberts & Rots 1973; Kyazumov 1984; Burstein & Rubin 1985). Average RC shapes within the optical radii r_{opt} of late-type spirals have been studied extensively by Persic and collaborators (Persic & Salucci 1988, 1990a,b, 1991; Persic et al. 1996), using long-slit optical spectra. In their “Universal Rotation Curve” (URC) model, systems with absolute *I*-band luminosities $M_I^o \lesssim -22.0$ ($V_{\text{rot}} \gtrsim 200 \text{ km s}^{-1}$) have RCs that peak at $\sim 0.8r_{\text{opt}}$ and decline at larger galactocentric radii r . However, the URC parametrization tends to underpredict the outer RC amplitudes of high surface brightness systems (e.g. Courteau 1997). Average optical RC shapes for a much larger sample of spirals have since been compiled by Catinella et al. (2006), who find no evidence for declining RCs within r_{opt} even in the most luminous systems.

Neutral hydrogen (H I) is an effective tracer of late-type spiral galaxy kinematics beyond r_{opt} , since the H I disk is typically 50% larger than the stellar one (e.g. Broeils & Rhee 1997). The outer RC shapes derived from H I observations are typically more uncertain than those in the optical, however, because measurements of the inclination i are required to correct observed velocities for

¹ Present address: Jansky Fellow, National Radio Astronomy Observatory; Department of Physics and Astronomy, Rutgers, the State University of New Jersey, 136 Frelinghuysen Road, Piscataway, NJ, 08854; spekkens@physics.rutgers.edu

² National Astronomy and Ionosphere Center (NAIC), Cornell University, Ithaca, NY, 14853; riccardo@astro.cornell.edu. NAIC is operated by Cornell University under cooperative agreement with the National Science Foundation (NSF).

TABLE 1
BASIC PROPERTIES OF THE FAST ROTATOR SAMPLE

Galaxy	α_c (J2000)	δ_c (J2000)	type	V_\odot (km s^{-1})	D (Mpc)	
(1)	(2)	(3)	(4)	(5)	(6)	
NGC 1324	03 25 01.6	-05 44 42	Sb:	(3)	5672	79.4
UGC 2849	03 45 32.9	+44 51 18	Scd:	(6)	8142	116.0
ESO 563G21	08 47 16.4	-20 02 09	SAbc: sp	(4)	4581	70.1
NGC 2862	09 24 55.3	+26 46 29	Sb	(3)	4110	63.0
NGC 2955	09 41 16.6	+35 52 56	(R')SA(r)b	(3)	7008	105.0
IC 4202	13 08 31.5	+24 42 01	Sbc	(4)	7127	103.9
NGC 6195	16 36 32.6	+39 01 37	Sb	(3)	9022	130.5
UGC 11455	19 29 56.0	+72 06 44	Sc	(6)	5393	76.1

NOTE. — Col. (1): NGC/IC designation where available, else UGC/ESO number. Cols. (2)-(3): Galaxy coordinates (J2000). Col.(4): Morphological type, as given in the Nasa Extragalactic Database (NED). Corresponding RC3 type numbers given in parentheses (de Vaucouleurs et al. 1991). Col. (5): Heliocentric (optical) radial velocity, derived from archived single-dish spectra as in Springob et al. (2005). Col. (7): Distance corresponding to V_\odot , computed using α , δ and $H_0 = 70 \text{ km s}^{-1} \text{ Mpc}^{-1}$.

viewing geometry. While i is relatively constant across the optical disks of spirals and can be robustly measured from photometry, warps are common in the H I layer beyond r_{opt} (e.g. García-Ruiz et al. 2002) and variations in i in these regions can be difficult to constrain with available data (e.g. §4.2). Nonetheless, the majority of spirals have H I RCs that are relatively flat in their outer parts (e.g. Bosma 1978, 1981a,b), though the possibility that many RCs become Keplerian within $r \sim 3r_{opt}$ cannot be ruled out (Honma & Sofue 1997). There are also some unambiguous detections of decreasing RCs beyond r_{opt} (see the compilation by Honma & Sofue 1997). Two such cases are NGC 2683 and NGC 3521, where large ($\sim 50 \text{ km s}^{-1}$, or $0.25 V_{rot}$) declines are detected between 1 and 3 r_{opt} (Casertano & van Gorkom 1991, hereafter CvG91). CvG91 also find correlations between the logarithmic RC slopes beyond $2/3r_{opt}$ and the rotation amplitudes, scale-lengths, surface brightnesses, and morphological types for a diverse sample of late-type spirals with reliable H I RCs. These trends suggest that the RCs of massive systems – compact, high surface brightness ones in particular – decrease in amplitude or decline steadily beyond r_{opt} .

Observationally, spirals with $V_{rot} \gtrsim 350 \text{ km s}^{-1}$ are rare, particularly for later morphological types. While V_{rot} for the fastest known rotator in the local Universe exceeds 500 km s^{-1} (UGC 12591; Giovanelli et al. 1986), the distribution of H I spectral line widths in large samples of spirals truncates abruptly near $W \sim 2V_{rot} \sim 550 \text{ km s}^{-1}$ (e.g. Koribalski et al. 2004; Springob et al. 2005). Elliptical galaxies exhibit a similar upper limit to their central velocity dispersions, which can be understood in the context of the Λ CDM structure formation paradigm provided that the stars in their cores formed prior to $z \sim 6$ and behave like collisionless particles thereafter (Loeb & Peebles 2003). There is no analogous explanation for the upper bound to V_{rot} in spirals. One possibility is that the progenitors of spirals with $V_{rot} > 350 \text{ km s}^{-1}$ seldom form long-lived disks. In particular, if the latter are stabilized against bar formation by massive halos (Ostriker & Peebles 1973, Efstathiou

et al. 1982; Christodoulou et al. 1995a,b) and their baryonic components scale with parent halo masses and angular momenta (e.g. Dalcanton et al. 1997; Mo et al. 1998; de Jong & Lacey 2000), then a stability criterion of the form $\lambda \gtrsim m_d$ arises, where λ is the halo spin parameter and m_d is the cold baryon fraction (Mo et al. 1998). Since collisionless halos with $\lambda > 0.1$ are rare (e.g. Bullock et al. 2001), massive systems that retain most of their baryons during galaxy formation would seldom have large enough λ to form stable disks. In this scenario, massive spirals have large λ . The angular momentum distributions of local fast rotators probe the stability of disks in high-mass systems, and thus this explanation for the observed upper limit to V_{rot} .

We have obtained H I aperture synthesis observations for 8 late-type, rapidly rotating spirals in the local Universe, each with I -band photometry and optical spectroscopy archived in the SFI++ database maintained at Cornell University. We combine the optical and H I kinematics to produce hybrid RCs for each system, that have arcsecond resolution within r_{opt} and that extend beyond the stellar disk into the region where dark matter dominates the potential. In a future paper, we will use these data to constrain the dark and luminous contributions to the derived kinematics, and to compute the angular momentum distributions and λ for a wide range of baryon mass-to-light ratios (Spekkens & Giovanelli 2006, in preparation). Here, we present our observations and concentrate on deriving accurate optical+H I RCs that will underpin our models. We also compare the outer RC shapes obtained to those of the systems compiled by CvG91, and re-evaluate the evidence for correlations between these shapes and other galaxy properties with the fast rotator and CvG91 samples combined.

The organization of this paper is as follows. We describe the sample selection and present available SFI++ catalog photometry and optical kinematics in §2. We present the aperture synthesis H I observations and related analysis in §3, and describe the derivation of hybrid optical/H I RCs in §4. We summarize our results and discuss the outer RC shapes of the fast rotator sample in

§5. Notes on individual systems as well as H I channel maps of the detected emission are given in Appendix A.

Unless otherwise stated, we convert angular sizes to physical scales by adopting $H_0 = 70 \text{ km s}^{-1} \text{ Mpc}^{-1}$, and give radial velocities following the heliocentric, optical definition.

2. SAMPLE SELECTION AND SFI++ DATA

The fast rotator sample is selected from the SFI++ database maintained at Cornell University. The SFI++ is a compilation of I -band photometry and V_{rot} measurements for several thousand late-type spiral galaxies, optimized for studies of the large-scale mass distribution in the local Universe. The catalog includes several datasets published by our group (Haynes et al. 1999a, hereafter H99; Dale & Giovanelli 2000, and references therein; Vogt et al. 2004; Springob et al. 2005; Catinella et al. 2005, hereafter C05) as well as newly acquired data, and is fully described elsewhere (Masters 2005; Springob 2006; Springob et al. 2006, in preparation).

Sample candidates have both single-dish H I profiles and long-slit optical spectroscopy archived in the SFI++. Of these, we select 8 galaxies with the largest V_{rot} that a) show no evidence for interactions, close companions or disturbed optical morphologies, and b) have H I line strengths and optical sizes suitable for H I aperture synthesis observations with the Very Large Array³ (VLA). The basic properties of the fast rotator sample are presented in Table 1.

The mean rotational velocity for the sample galaxies is $V_{rot} \sim 275 \text{ km s}^{-1}$: they are therefore at the high-mass end of the local spiral galaxy population. Unlike the compilation of Saglia & Sancisi (1988), however, we find no evidence for discrepancies between the system properties and the velocity, size, magnitude, and surface brightness scaling relations for the SFI++ (Spekkens 2005). Moreover, despite their large absolute scales both the global gas fractions and surface densities of the galaxies are within the ranges expected for normal spirals of the same morphological types (see §3.1.1). The fast rotator sample thus represents an extreme of the normal spiral galaxy population rather than a separate class of object.

2.1. I -band Images and Photometry

I -band images and photometry for the sample are mined from the SFI++, and a thorough description of the data acquisition and reduction techniques can be found in H99. Below, we summarize this procedure and describe our bulge-disk decomposition technique in some detail.

The I -band images were obtained during a series of observing runs by our group between 1988 and 1997, using the 1.3m McGraw-Hill telescope at the Michigan-Dartmouth-MIT Observatory⁴ as well as the 0.9m telescopes at the Kitt Peak National Observatory and the

³ The Very Large Array is a facility of the National Radio Astronomy Observatory (NRAO). The NRAO is a facility of the NSF, operated under cooperative agreement with Associated Universities, Inc.

⁴ The MDM Observatory is jointly operated by the University of Michigan, Dartmouth College, and the Massachusetts Institute of Technology on Kitt Peak, Arizona.

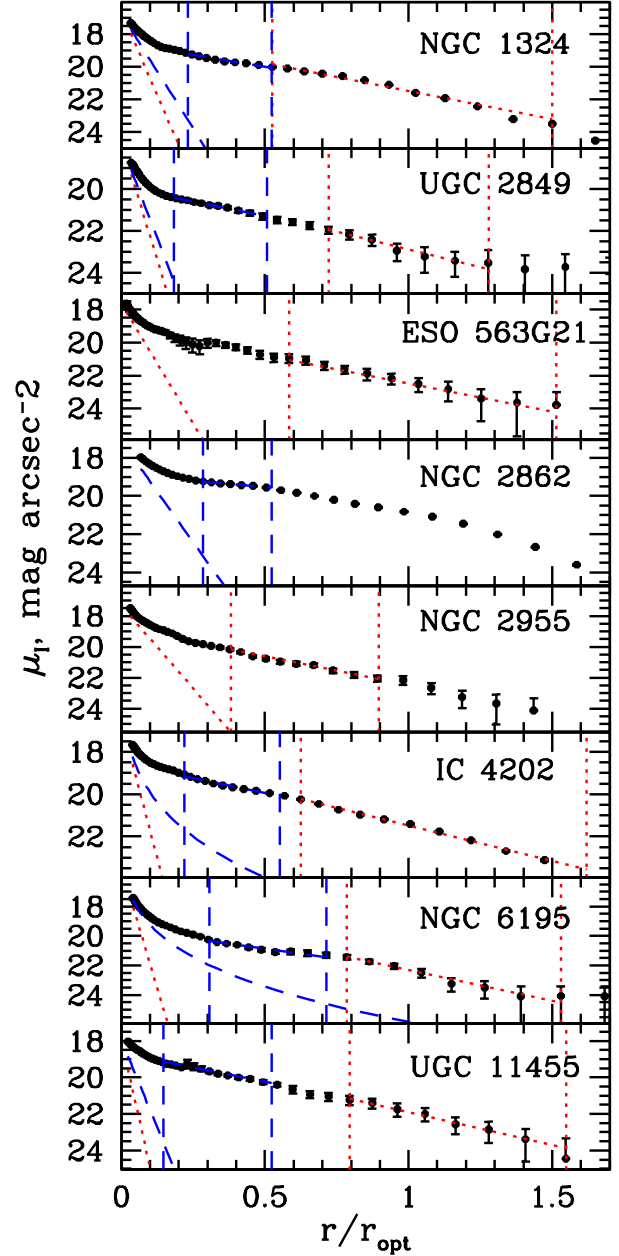


FIG. 1.— I -band surface brightness profiles for the fast rotator sample. In each panel, points bracketed by the vertical dotted lines constrain the exponential disk in the “minimal” bulge computation, while points bracketed by the dashed vertical lines constrain the exponential disk in the “maximal” bulge computation. In each case, the disk fits are given by the lines through the points, and the resulting minimal and maximal bulge fits are represented by the dotted and dashed diagonal lines, respectively. A color version of this figure is available in the electronic edition of the Journal.

Cerro-Tololo Inter-American Observatory⁵. The images were homogeneously calibrated using standard procedures within the IRAF/STSDAS environment⁶ in the

⁵ The Kitt Peak National Observatory and Cerro-Tololo Inter-American Observatory are part of the National Optical Astronomy Observatories (NOAO), operated by Associated Universities for Research in Astronomy (AURA), Inc., under a cooperative agreement with the NSF.

⁶ IRAF is distributed by NOAO, which is operated by AURA

TABLE 2
I-BAND PHOTOMETRY

NGC/IC	M_I^o mag	r_d^o (kpc)	$\mu_{e,I}$ (mag asec $^{-2}$)	$B_T^0 - I$ (mag)	r_{opt} (kpc)	r_{235}^o (kpc)	θ_d ($^{\circ}$)	ϵ_{psd}	i_d ($^{\circ}$)	B/D_{min}	B/D_{max}
(1)	(2)	(3)	(4)	(5)	(6)	(7)	(8)	(9)	(10)	(11)	(12)
NGC 1324	-23.6	5.6	18.7	...	19.7	27.2	139.9 ± 0.7	0.72 ± 0.04	78	0.02	0.06
UGC 2849	-23.5	6.2	19.0	...	21.0	20.5	82 ± 2	0.55 ± 0.2	66	0.02	0.04
ESO 563G21	-23.6	6.9	19.1	1.36	25.7	28.1	165.9 ± 0.5	0.77 ± 0.02	83	0.06	0.06
NGC 2862	-23.2	4.4	18.6	1.77	15.0	22.6	114.4 ± 0.9	0.79 ± 0.01	86	0.0	0.04
NGC 2955	-23.3	4.9	18.7	...	20.2	23.5	159 ± 5	0.42 ± 0.06	56	0.3	0.3
IC 4202	-23.1	4.5	18.8	1.95	16.7	21.2	142.0 ± 0.1	0.82 ± 0.01	90	0.01	0.07
NGC 6195	-23.7	6.1	18.8	1.76	23.0	26.2	39 ± 5	0.5 ± 0.1	62	0.03	0.3
UGC 11455	-23.3	5.8	19.1	2.12	21.0	23.7	62 ± 1	0.83 ± 0.02	90	0.0	0.01

NOTE. — Col. (2): Absolute I -band magnitude computed using D from Table 1, corrected for internal and galactic extinction. Col.(3): Exponential disk scale-length, corrected to a face-on perspective. Col. (4): I -band effective central surface brightness, computed using M_I^o from col. (2) and r_d^o from col. (3). Col. (5): $B - I$ color estimated using B_T^0 from the RC3 (de Vaucouleurs et al. 1991) and M_I^o from col. (2). Col. (6): Optical radius, within which 83% of the total I -band light is contained. Col. (7): Radius of the 23.5th mag asec $^{-2}$ isophote, corrected to a face-on perspective. Col. (8): Average position angle in the disk fitting region. Col (9): Average ellipticity ($\epsilon_{psd} = 1 - b/a$, where a and b are major and minor axes) in the disk fitting region. Col. (10): Average inclination in the disk fitting region, computed from col. (9) assuming an intrinsic axial ratio $q = 0.2$. Col. (11): “Minimum” ratio of bulge light to disk light, from decomposition with the exponential disk of col. (2). Col. (12): “Maximum” ratio of bulge light to disk light, from decomposition with a disk fit in the “dip” of the surface brightness profile (see text).

TABLE 3
OPTICAL AND H I KINEMATICS

NGC/IC	ϕ_l ($^{\circ}$)	r_{pe} (kpc)	V_{rot} (km s $^{-1}$)	S
(1)	(2)	(3)	(4)	(5)
NGC 1324	142	1.4	297 ± 4	-0.10
UGC 2849	72	2.3	270 ± 2	-0.04
ESO 563G21	164	4.1	308 ± 2	0.00
NGC 2862	114	5.0	272 ± 1	-0.11
NGC 2955	162	1.1	261 ± 5	-0.12
IC 4202	143	4.0	243 ± 1	-0.03
NGC 6195	45	1.1	250 ± 2	-0.03
UGC 11455	61	4.8	280 ± 9	0.02

NOTE. — Col. (2): Position angle of long axis of the slit in optical spectroscopy. Col. (3): Best fitting value of r_{pe} (eq. 1) to folded optical RCs. Col. (4): V_{rot} measured from hybrid optical+H I RC, corrected for projection effects using i_d from I -band photometry. Col. (5): Logarithmic outer RC slope, measured between $2/3 r_{235}^o$ from Table 2 and the outermost H I RC point.

manner described in H99.

Following calibration, the resulting image analysis was performed by M. P. Haynes for all galaxies. Photometric quantities were extracted by fitting concentric isophotal ellipses to the galaxy emission after masking nearby stars. The resulting surface brightness profiles are shown in Fig. 1. We define the optical radius r_{opt} as the radius within which 83% of the I -band profile light is contained (Persic et al. 1996); r_{opt} is equivalent to 3.2 scale-lengths in a pure exponential disk. The radius r_{235} of the 23.5th mag asec $^{-2}$ isophote is also measured. The average disk ellipticity ϵ_{psd} and position angle θ_d are determined by averaging measurements⁷ for ellipses in a

under cooperative agreement with the NSF. STSDAS is distributed by the Space Telescope Science Institute, which is operated by AURA under contract with the National Aeronautics and Space Administration.

⁷ For the highly-inclined systems ϵ_{psd} is taken as the maximum

region of the outer profile likely dominated by disk emission, as described by Giovanelli et al. (1994). The disk scale-length r_d is then derived from the slope of a linear fit to points in this region. The total apparent magnitude m_I is measured at $8r_d$, extrapolated to this level from the disk fit if required. The disk inclination i_d is then computed from ϵ_{psd} assuming an intrinsic axial ratio $q = 0.2$, and the photometric quantities are corrected to a face-on perspective (r_{235}^o, r_d^o, m_I^o) using the prescriptions of Giovanelli et al. (1995). We then compute the effective central surface brightness $\mu_{e,I}$ following CvG91, defined as the central surface brightness of a pure exponential disk with total luminosity m_I^o and scale-length r_d^o . The bulge contributions to the total I -band light are small for the fast rotators (see below), and thus $\mu_{e,I}$ approaches the extrapolated disk central surface brightness tabulated by H99. The derived photometric quantities for each system are given in Table 2.

The surface brightness profiles are then decomposed into disk and bulge contributions. To estimate the bulge component, we first subtract an exponential disk from the profile. The remaining light is then fit with both spherical exponential and de Vaucouleurs (1948) bulges, and the best fitting profile of the two is adopted as the bulge distribution. This bulge profile is then subtracted from the total surface brightness distribution, and the remaining light is assigned to the disk. The decomposition therefore preserves both the total I -band flux as well as the small-scale features of the profiles, which are assumed to stem from the disk.

The fraction of I -band flux assigned to the bulge clearly depends on the exponential disk first subtracted from the surface brightness distribution. However, the best fitting disk determined from one region of the surface brightness distribution may deviate significantly at other r in the profile, due to irregularities in the baryon distribution or to extinction effects. This is the case for many of the fast rotators, which show a “dip” in their

value in this region instead of the mean, since the isophote fitting method artificially decreases the latter (H99).

surface brightness distributions for $0.1r_{opt} \lesssim r \lesssim 0.4r_{opt}$ (Fig. 1). To estimate the range of reasonable bulge contributions for each galaxy, we therefore carry out the procedure described above starting from two distinct exponential disks: the fit from H99 yields a suitable “minimal” bulge contribution, while one estimated in the region of the profile dip produces a suitable “maximal” bulge contribution. Because of extinction effects in the surface brightness profiles, the actual bulge component is likely bracketed by these extremes.

The resulting bulge profiles are shown in Fig. 1. For each galaxy, points in between the vertical dotted lines are used to estimate the exponential disk in the minimal bulge computation (H99), while those bracketed by the dashed vertical lines produce the exponential disk in the maximal bulge estimate. The corresponding exponential disks are shown by the dotted and dashed lines through the points, and the resulting bulge fits are shown by the dotted and dashed diagonal lines at small r . Note that for NGC 2862 only the maximal bulge fit is plausible, while for ESO 563G21 and NGC 2955 the maximal and minimal estimates are identical; for these systems, a single bulge fit is therefore displayed. The resulting minimal and maximal ratios of bulge light to disk light are given in the last 2 columns of Table 2. As expected for late-type systems, the bulge component is dwarfed by the disk component even in the “maximum” bulge scenario. The bulge is thus not expected to contribute substantially to the observed kinematics, and it is likely reasonable to model the fast rotators as pure disk systems by assigning all of the I-band light to a thin axisymmetric component. The impact of these different decompositions on the inferred structure of each system will be fully explored at the mass modeling stage (Spekkens & Giovanelli 2006, in preparation).

For 5 of the 8 fast rotators, unmasked I -band images are archived in the SFI++ in addition to the photometry. For these systems, we determine a plate scale for each image by matching 15–20 stars in the vicinity of the galaxy to those in analogous Digitized Sky Survey⁸ (DSS) images and by solving for the pixel size, center and rotation angle. The positional accuracy of this linear solution is judged to be better than $1''$. The available I -band images are shown in greyscale in Figs 2a, 5a, and 7a–9a.

For clarity in the text that follows, we adopt θ and i as abbreviations for position angle and inclination, respectively, while θ_d and i_d specify the values from I -band photometry that are listed in cols. (8) and (10) of Table 2.

2.2. Long-Slit Optical Spectroscopy

The optical spectra for the fast rotator sample have also been mined from the SFI++. The data reduction and analysis are detailed in C05; here we summarize the procedure.

Long-slit optical spectra for 7 of the 8 fast rotators were obtained by our group between 1990 and 2002, using the

⁸ The DSS was produced at the Space Telescope Science Institute under U.S. Government grant NAG W-2166. The images of these surveys are based on photographic data obtained using the Oschin Schmidt Telescope on Palomar Mountain and the UK Schmidt Telescope. The plates were processed into the present compressed digital form with the permission of these institutions.

Double Spectrograph on the 200-inch Hale Telescope at Palomar Observatory⁹. The observing setup yielded a spectral resolution of $0.65 \text{ \AA pixel}^{-1}$ and a spatial resolution of $0.468'' \text{ pixel}^{-1}$ across a $2'' \times 125''$ slit. The long axis of the slit was placed at $\theta = \phi_l$ (Table 3) for each system. In general $\phi_l = \theta_d$ from the I -band images, within the uncertainties in the latter. The seeing full width at half-maximum (FWHM) was typically $1.5''$. The data were reduced and rotational velocities extracted using both standard IRAF packages as well as our own software. Where possible, the kinematics from the $\text{H}\alpha$ and N II lines were combined to form a single optical RC (C05). The RCs for NGC 2862, NGC 2955, IC 4202 and NGC 6195 presented here have been published by Vogt et al. (2004).

For ESO 563G21, we use the $\text{H}\alpha$ RC derived by Mathewson et al. (1992) obtained with a similar observing setup and reduction technique.

After calibration, all of the RCs were analyzed in the manner detailed in C05. Briefly, we fold each RC about the position determined from the best fitting URC to the points (Persic et al. 1996), and then fit a polyex function:

$$V_{pe}(r) = V_o \sin i (1 - e^{-r/r_{pe}})(1 + \beta r/r_{pe}), \quad (1)$$

where $V_o \sin i$ sets the amplitude of the fit, r_{pe} governs the inner RC slope, and β determines the outer RC slope. Values of r_{pe} for the fast rotators are given in Table 3. Since V_{rot} and the outer RC slope are better characterized by the hybrid RCs than the optical spectra alone, we do not tabulate the SFI++ V_o and β here.

Tables 2 and 3 demonstrate that the sample galaxies fall into two groups, depending on i_d and r_{pe} : NGC 1324, UGC 2849, NGC 2955, and NGC 6195 have $i_d \leq 78^\circ$ and $1.1 \leq r_{pe} \leq 2.3 \text{ kpc}$, whereas ESO 563G21, NGC 2862, IC 4202 and UGC 11455 have $i_d \geq 83^\circ$ and $r_{pe} > 4 \text{ kpc}$. The large r_{pe} in the latter galaxies likely result from extinction effects, which become more pronounced with increasing i (e.g. Giovanelli & Haynes 2002). The fast rotators thus divide into an intermediate i sub-sample and a highly inclined sub-sample.

The optical RCs for the fast rotator sample, corrected for projection effects using i_d and resampled to a resolution of approximately $2''$ ($3.2''$ for ESO 563G21) to reflect the seeing conditions, are given by the triangles in Figs. 11–12. The errorbars on each point reflect either the accuracy with which the emission centroid could be determined in the optical spectrum, or an imposed minimum of $2/\sin i_d \text{ km s}^{-1}$.

3. APERTURE SYNTHESIS H I OBSERVATIONS

The sample galaxies were observed with the VLA in its C configuration in separate runs during July – August 2001 and October – December 2002, except for ESO 536G21 which was observed in BC configuration in October 2002 to prevent excessive antenna shadowing at low latitudes. During each run the galaxy was targeted in 25–35 minute intervals, separated by 3–5 minute phase calibrator observations. The flux calibrator, also used as

⁹ The Hale Telescope, Palomar Observatory, is operated under a collaborative agreement between the California Institute of Technology, its divisions Caltech Optical Observatories and the Jet Propulsion Laboratory (operated for NASA), and Cornell University.

TABLE 4
H I OBSERVING AND MAP PARAMETERS

NGC/IC	TOS (min)	Natural Weighting			Uniform Weighting		Overlap (7)
		Beam @ ϕ ($'' \times '' @ {}^\circ$)	$\bar{\sigma}$ (mJy/beam)	Beam @ ϕ ($'' \times '' @ {}^\circ$)	$\bar{\sigma}$ (mJy/beam)		
NGC 1324	264	23 \times 17 @ -10	0.36	17 \times 14 @ -14	0.45	4	
UGC 2849	273	22 \times 17 @ 6	0.36	17 \times 13 @ 13	0.43	2	
ESO 563G21	171	22 \times 12 @ 3	0.48 ^a	13 \times 8 @ 74	0.57 ^a	0	
NGC 2862	307	18 \times 17 @ -14	0.25	14 \times 14 @ -23	0.30	4	
NGC 2955	206	21 \times 18 @ 82	0.33	16 \times 14 @ -87	0.40	8	
IC 4202	243	20 \times 15 @ -7	0.31	15 \times 13 @ -9	0.36	6	
NGC 6195	378	18 \times 17 @ -77	0.28	14 \times 13 @ -71	0.33	2	
UGC 11455	314	20 \times 16 @ -10	0.28	15 \times 13 @ -9	0.32	3	

NOTE. — Col. (2): Integration time on-source, before editing. Cols. (3) - (4): Synthesized beam size and position angle, and mean RMS map noise per channel in the naturally weighted cubes. Cols. (5) - (6): Synthesized beam size and position angle, and mean RMS map noise per channel in the uniformly weighted maps. Col. (7): Number of overlapping channels near datacube center; see text.

^a σ at $v = 4389 \text{ km s}^{-1}$ is 10% higher than this value; see text.

a bandpass calibrator, was observed at both the start and the end of each run. The raw on-source integration time for each system is listed in Table 4.

The sample galaxies were at the pointing center of their corresponding runs, resulting in sky coverage within a primary beam FWHM=31.3' centered on each source. To adequately sample the full width of the integrated H I line for the fast rotators, two 3.125 MHz bandpasses were staggered about their single-dish profile centers. This yielded contiguous frequency coverage across each source in 97 kHz spectral channels, as well as sufficient baseline to subtract continuum emission. The bandpasses overlapped near the band center, with the number of duplicate channels determined from the net bandwidth required for each observation.

The data were calibrated using the Astronomical Image Processing System¹⁰ (AIPS; Napier et al. 1993). For each run, standard editing, flux, phase and bandpass calibration routines were applied separately to the 2 polarizations of each bandpass (Rupen 1999 and references therein). The bandpasses were then joined and the data in the overlapping channels averaged to produce a single band; the number of overlapping channels at the band center for each system is given in Table 4. In most cases the continuum emission could be subtracted via linear fits to the real and imaginary Fourier components in the line-free frequency channels (e.g. van Langevelde & Cotton 1990). For NGC 1324, NGC 2955 and IC 4202, models of strong continuum sources far from the pointing center were first subtracted (Ekers & van Gorkom 1984; van Gorkom & Ekers 1989).

Following the data reduction, strong radio frequency interference (RFI) was discovered in 1–2 channels near 1400 MHz in the ESO 563G21 and NGC 2862 datacubes. This well-known VLA birdie is caused by correlated noise from the 7th harmonic of the 200 MHz L-band local oscillator in the shortest east-west baselines, where the fringe rate is small (Bagri 1996). We excise this RFI following the method of Spekkens et al. (2004). We remove baselines with east-west projections less than 25 m and 17 m

in all spectral channels and clip contaminated channels above 0.7 Jy and 1.0 Jy for ESO 563G21 and NGC 2862, respectively. In all, the excision flags less than 5% of the available baselines. We checked for possible biases from this editing by examining residual datasets in the same manner as described in the appendix of Spekkens et al. (2004), and found no evidence for any systematic flux loss. We measure an increased RMS map noise σ of 10% at 4389 km s⁻¹ in the ESO 563G21 datacube as a result of the clipping, but find no change in the RFI-excised channels of the NGC 2862 datacube.

After calibration the data were imaged using both natural and uniform weighting schemes to emphasize H I structures on different spatial scales. The emission in each cube was then CLEANed (Clark 1980) of sidelobe contamination and corrected for the attenuation of the primary beam. The synthesized beam parameters and the average RMS noise $\bar{\sigma}$ per channel for the calibrated datasets are given in Table 4. In general, the map noise σ is $\sim 10\%$ lower than $\bar{\sigma}$ in the overlap channels. This gain in sensitivity is less than the factor $\sqrt{2}$ anticipated from averaging two independent channels together, because of correlated noise from continuum subtraction and decreased sensitivity near the bandpass edge.

3.1. H I Data Presentation

The H I data for the fast rotators are presented in Figs 2–9, and their properties are summarized in Table A6. Channel maps as well as notes for individual systems are in Appendix A.

In the interest of deriving high-quality kinematics in the outer H I-rich parts of the disks, we trade sensitivity for angular resolution and analyze the uniformly weighted maps for all the fast rotators except ESO 563G21, where the S/N is too low with uniform weighting. We also perform a cursory search for companions in the naturally weighted cubes: we make detections in the vicinity of half the sample galaxies, and half again are previously uncatalogued. The properties of the detected companions are given in Table 5. Throughout, we use a combination of AIPS and Groningen Image Pro-

¹⁰ <http://www.aoc.nrao.edu/aips/>

cessing System¹¹ (GIPSY) routines to manipulate and display the data.

3.1.1. H I Morphologies and Global Properties

The contours in Figs. 2a–9a show total intensity (zeroth moment) maps for the fast rotators, obtained by summing the detected emission along the frequency axis. To reduce the noise in the maps we use blanked versions of the datacubes shown in Appendix A: we first smooth the data to half the spatial resolution listed Table 4, and blank the full resolution cube at all locations with emission less than the mean RMS $\bar{\sigma}$ of the blanked cubes. We then flag the resulting full resolution cube interactively, keeping only emission associated with the galaxy of interest and appearing in 2 consecutive channels. The H I contours in Figs. 2a–9a are overplotted on archived *I*-band images where available (see §2.1), or else on DSS images.

Figs. 2b–9b show velocity fields for each of the fast rotators; their derivation is discussed in detail in §3.1.2.

Figs. 2c–9c show the line intensities as a function of heliocentric radial (optical) velocity for the fast rotators and the detected companions. The 1σ errorbars on each point include contributions from $\bar{\sigma}$ over the emission region as well as a 5% calibration uncertainty. The integrated line intensities $\int Idv$ obtained by summing these global profiles along the velocity axis are given in col. (2) of Table A6.

For each system, we compute the raw velocity width $W \sin i$ by fitting straight lines to the datapoints on the outer edges of the global profile horns, and measuring the width from these fits at 50% of the horn peak. We correct for instrumental broadening by subtracting one channel width from this measurement, in accordance with the recommendation of Springob et al. (2005) from their simulations. Estimates of $W \sin i$ for each fast rotator, and the corresponding profile mid-points V_{sys} are in Table A6. The errors on $W \sin i$ correspond to half the difference between the listed values and those measured at 20% of the profile peaks using the same technique. We do not correct for ISM turbulence, estimated to be on the order of a few km s^{-1} and therefore small compared to both $W \sin i$ and its uncertainty (Tully & Fouqué 1985; Lavezzi & Dickey 1997; Springob et al. 2005). In general there is good agreement with published single-dish values (see Appendix A), and we make no short-spacings corrections to our data.

The H I mass M_{HI} obtained from the global profile is given in col. (5) of Table A6, and is computed assuming an optically thin disk:

$$M_{HI} = (2.36 \times 10^5) D^2 \int Idv M_{\odot}, \quad (2)$$

where D is in Mpc and $\int Idv$ is in Jy km s^{-1} .

Radial surface density profiles $\Sigma_{HI}(r)$ are typically obtained by averaging the H I brightness in concentric rings as in Warner et al. (1973), but this method yields erroneous results for systems that are poorly resolved along their major or minor axes (Bosma 1978; Swaters et al. 2002). We therefore adopt the method of Warmels (1988), and integrate the total intensity map for each

system along the *I*-band minor axis to produce “strip integrals”. A beam-corrected, face-on estimate of $\Sigma_{HI}(r)$ is then derived from the strip integrals under the assumption of axisymmetry, using Lucy’s (1974) iterative deconvolution technique for an initial guess of the distribution shape (see also Swaters et al. 2002). The resulting $\Sigma_{HI}(r)$ for each system are shown in Figs. 2d–9d for the approaching side (crosses), the receding side (triangles), and the average of both sides (points) of the H I intensity map in Figs. 2a–9a. We adopt the outermost point at which $\Sigma_{HI}(r) = 1 M_{\odot} \text{ pc}^{-2}$ in the averaged profile as the H I radius r_{HI} . The ratio r_{HI}/r_{opt} for each system is given in Table A6.

The total dynamical mass is computed assuming spherical symmetry:

$$M_T = (6.78 \times 10^4) r_{HI} D V_{rot}^2 M_{\odot}, \quad (3)$$

where r_{HI} is in arcminutes and V_{rot} is in km s^{-1} . We note that collisionless Λ CDM halos are typically oblate with intrinsic axial ratios $0.5 \lesssim q \lesssim 0.7$ (e.g. Jing & Suto 2002). However, a mild halo ellipticity has little impact on the derivation of M_T (Lequeux 1983), and therefore eq. 3 is adequate given the uncertainties in the input parameters.

An estimate for the dynamical mass is obtained from eq. 3 for the approaching and receding sides of each fast rotator separately. We define r_{HI} such that $\Sigma_{HI}(r_{HI}) = 1 M_{\odot} \text{ pc}^{-2}$, and take V_{rot} as the plateau of the hybrid RCs near r_{opt} (§4). The results are then averaged to produce M_T , listed in Table A6. We adopt an uncertainty on M_T equal to the sum in quadrature of half the difference between M_T for the approaching and receding sides, and the uncertainty obtained by propagating errors in r_{HI} and V_{rot} through eq. 3. The average value of V_{rot} for the sample galaxies is given in Table 3, where errorbars represent half the difference between values obtained for the approaching and receding sides.

We also list the parameters of form M_{HI}/M_T , $\sigma_{HI} = M_{HI}/\pi r_{HI}^2$ and $\sigma_T = M_T/\pi r_{HI}^2$ in Table A6. They demonstrate that despite their large absolute scale, the fast rotators have the same average properties as normal spirals: while M_{HI} and M_T for all of the fast rotators exceed the 75th percentiles of the volume-limited RC3-LSc sample of Roberts & Haynes (1994), the values of M_{HI}/M_T , σ_{HI} and σ_T lie within the expected ranges for their morphological types¹².

The global properties of the detected companions are given in Table 5. Estimates of $\int Idv$, V_{sys} , $W \sin i$, and M_{HI} are computed in the same manner as for the fast rotators, adopting D of the parent system in eq. 2. For M_T we approximate $r_{HI} = 1.5 \times a/2$ and $V_{rot} = W \sin i / \cos^{-1}(b/a)$, where a and b are the optical major and minor axis diameters. Given the uncertain morphologies, poor resolution and limited S/N of the detected companions, M_T should be regarded as only a rough approximation to the dynamical masses of these systems.

3.1.2. H I Kinematics

¹² We adjust the values in Table A6 to account for the different cosmology and parameter definitions adopted in Roberts & Haynes (1994) before making the comparison.

¹¹ <http://www.astro.rug.nl/~gipsy>

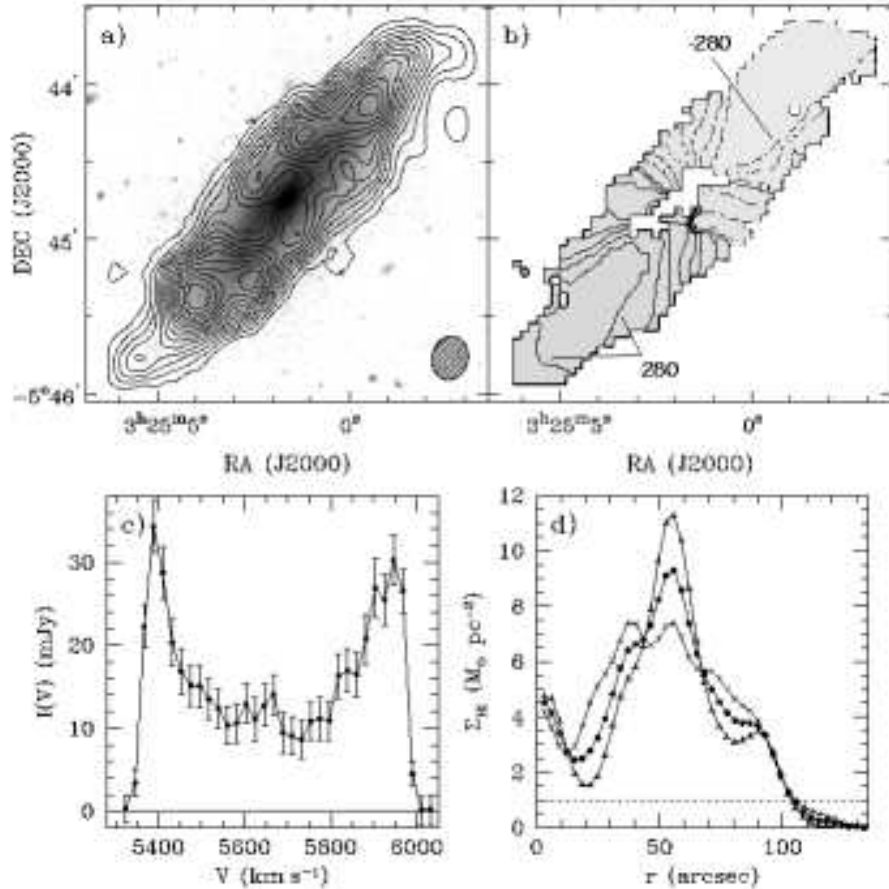


FIG. 2.— H I properties of NGC 1324. a) Uniformly weighted H I total intensity contours overplotted on an *I*-band image. Contours range from $3.8 \times 10^{20} \text{ cm}^{-2}$ to $3.0 \times 10^{21} \text{ cm}^{-2}$ in $2.0 \times 10^{20} \text{ cm}^{-2}$ intervals. The synthesized beam is shown in the bottom right corner. b) MET velocity field (shaded region). Contours are plotted in 40 km/s increments relative to V_{sys} in Table A6, with solid lines on the receding side and dotted lines on the approaching side. Some contours are labelled in km s^{-1} for clarity. c) Global profile. Errorbars reflect 1σ uncertainty contributions from σ over the emission region and a 5% calibration error. d) Radial surface density profile $\Sigma_{HI}(r)$ corrected to a face-on perspective for the approaching side (crosses), the receding side (triangles), and their average (points). The dotted line shows $1M_{\odot} \text{ pc}^{-2}$.

Rather than adopting a traditional intensity weighting (or first moment; Warner et al. 1973) scheme to derive the velocity fields in Figs 2b–9b, we use G04’s Modified Envelope Tracing (MET). We describe the technique, its advantages over moment analyses, and its application to our data here. For clarity in what follows, let $V_{mom1}(\alpha, \delta)$ and $V_{MET}(\alpha, \delta)$ refer to radial velocities at a sky position (α, δ) derived using the first moment and MET techniques, respectively. Quantities as a function of r instead of (α, δ) are measured along the major axis of the system, and the kinematic center is at $r = 0$. We use $V_{obs}(r)$ to denote the radial velocity adopted at r . For an axisymmetric, rotationally supported disk, $V_{obs}(r) = V_c(r) \sin i$, where $V_c(r)$ is the circular velocity of the system at r . We wish to derive $V_{obs}(r)$ that approach $V_c(r) \sin i$.

First moment velocities are obtained by weighting each contribution by its intensity $I(\alpha, \delta, v)$:

$$V_{mom1}(\alpha, \delta) = \frac{\int I(\alpha, \delta, v) v dv}{\int I(\alpha, \delta, v) dv} , \quad (4)$$

where v represents the frequency or velocity axis. When the line profiles $I(\alpha, \delta, v)$ are symmetric about the profile peaks the first moment yields reliable estimates of

$V_c(r) \sin i$, as do methods that fit gaussians or find centroids (see Sofue & Rubin 2001 for a review). In highly inclined or poorly resolved disks, however, a single line of sight will intercept lower-velocity emission in addition to gas at $V_c(r) \sin i$: this results in profiles that are skewed toward V_{sys} , biasing $V_{mom1}(\alpha, \delta)$ lower than $V_c(\alpha, \delta)$.

The impact of this bias in our data is illustrated in Fig. 10. In the left panel, the points show different estimates of the raw RC for the receding side of IC 4202: the triangles denote $V_{mom1}(r_i)$ computed from eq. 4. The solid circles show $V_{obs}(r_i)$ derived from the optical spectroscopy described in §2.2, for which beam smearing effects are negligible. In the absence of observing and data reduction biases, we expect $V_{obs}(r_i)$ derived from H I to resemble that derived from H α in the region probed by both tracers. The right panel shows the spectral profile $I(r', v)$ extracted at the location corresponding to the long-dashed vertical line in the left panel. The lower dashed, horizontal line denotes $V_{mom1}(r')$ derived for that profile. This value is clearly biased towards V_{sys} ($= 0$ in this plot) relative to the profile peak, and as a result there is a significant discrepancy between $V_{mom1}(r')$ and $V_{obs}(r')$ estimated from optical spectroscopy.

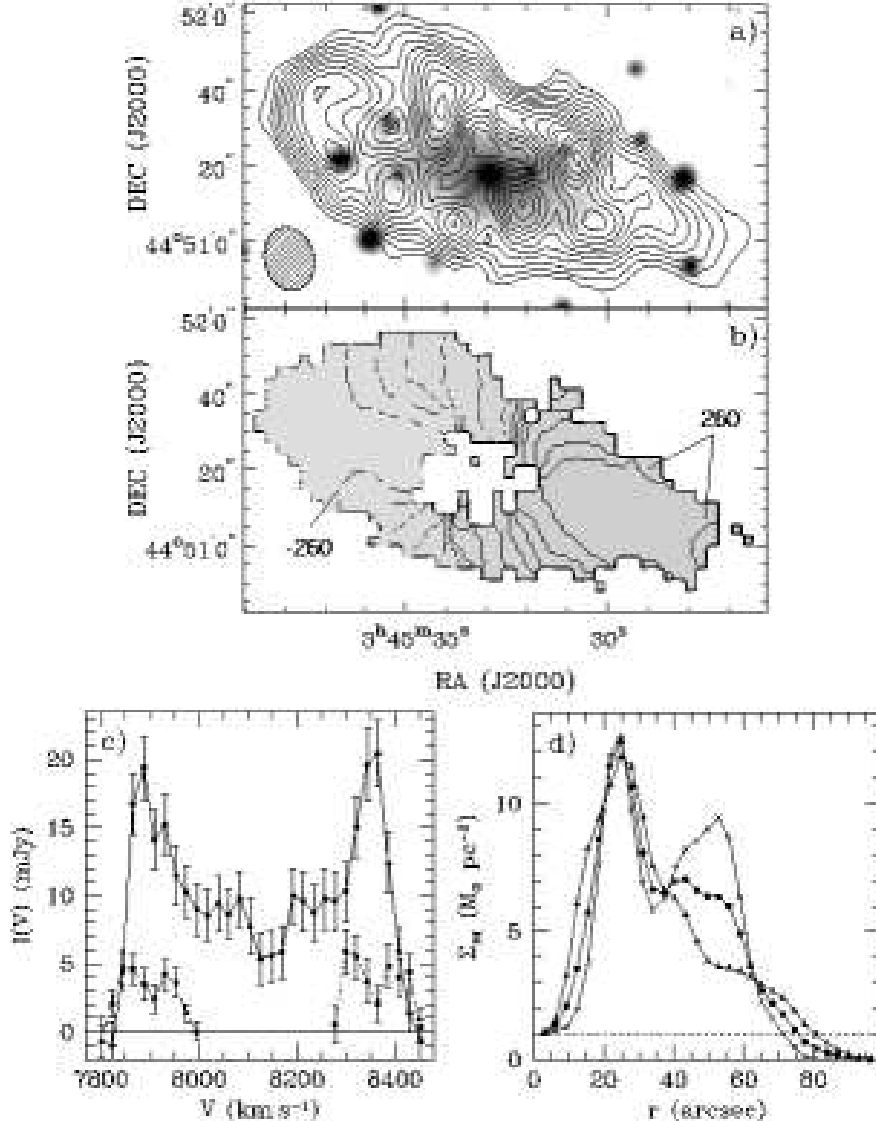


FIG. 3.— Same as in Fig. 2, but for UGC 2849. In a), H I contours range from $4.7 \times 10^{20} \text{ cm}^{-2}$ to $2.4 \times 10^{21} \text{ cm}^{-2}$ in $1.4 \times 10^{20} \text{ cm}^{-2}$ intervals, overplotted on a DSS image.

We therefore adopt the MET method of G04 to derive velocity fields for the fast rotator sample. For emission tracing the kinematics of an inclined rotating disk, the extreme-velocity side of $I(\alpha, \delta, v)$ (that farthest from V_{sys}) represents $V_c(\alpha, \delta)$ modulated by the telescope response and ISM turbulence. An estimate of the latter can therefore be derived from a “terminal velocity” $V_t(\alpha, \delta)$, which G04 define as the velocity at half-maximum of a half-gaussian fit to the extreme-velocity side of the profile. The velocity field is then given by:

$$V_{MET}(\alpha, \delta) = V_t(\alpha, \delta) - 0.5\sqrt{(\Delta V_{ISM})^2 + (\Delta V_{obs})^2} . \quad (5)$$

In eq. 5, ΔV_{ISM} accounts for turbulent broadening of the ISM and ΔV_{obs} corrects for the instrumental broadening of the system. Following G04 we assume a constant velocity dispersion $\sigma_{ISM} = 10 \text{ km s}^{-1}$ with $\Delta V_{ISM} = 2.35\sigma_{ISM}$, and set ΔV_{obs} to the spectral channel width in km s^{-1} . For our datasets ΔV_{ISM} and ΔV_{obs} have similar amplitudes, and the $V_{MET}(\alpha, \delta)$ obtained are in-

sensitive to changes in σ_{ISM} in the range $7 \text{ km s}^{-1} \lesssim \sigma_{ISM} \lesssim 12 \text{ km s}^{-1}$ (Kamphuis 1993).

Phenomena other than turbulence and spectral resolution can alter the extreme-velocity side of the profiles. Some of these stem from the galaxy itself, such as outflows or high velocity cloud (HVC) analogs. These “internal” factors are of little concern in our sample, since we are interested mainly in the outer H I disk and do not have the sensitivity to detect putative HVCs (Pisano et al. 2004). One should also account for spatial beam smearing in regions where the RC derivative is large: this will broaden the extreme-velocity side of the profile since along a line of sight, gas at larger r (higher $V_c(r)$) will be included via convolution by the synthesized beam. The $V_{MET}(r)$ derived from eq. 5 then are, in principle, upper limits to $V_c(r) \sin i$ (e.g. Sancisi & Allen 1979). However, minor axis resolution effects are so severe in the inner regions of the fast rotator disks that eq. 5 under-estimates $V_c(r) \sin i$ even when beam smearing is neglected. This

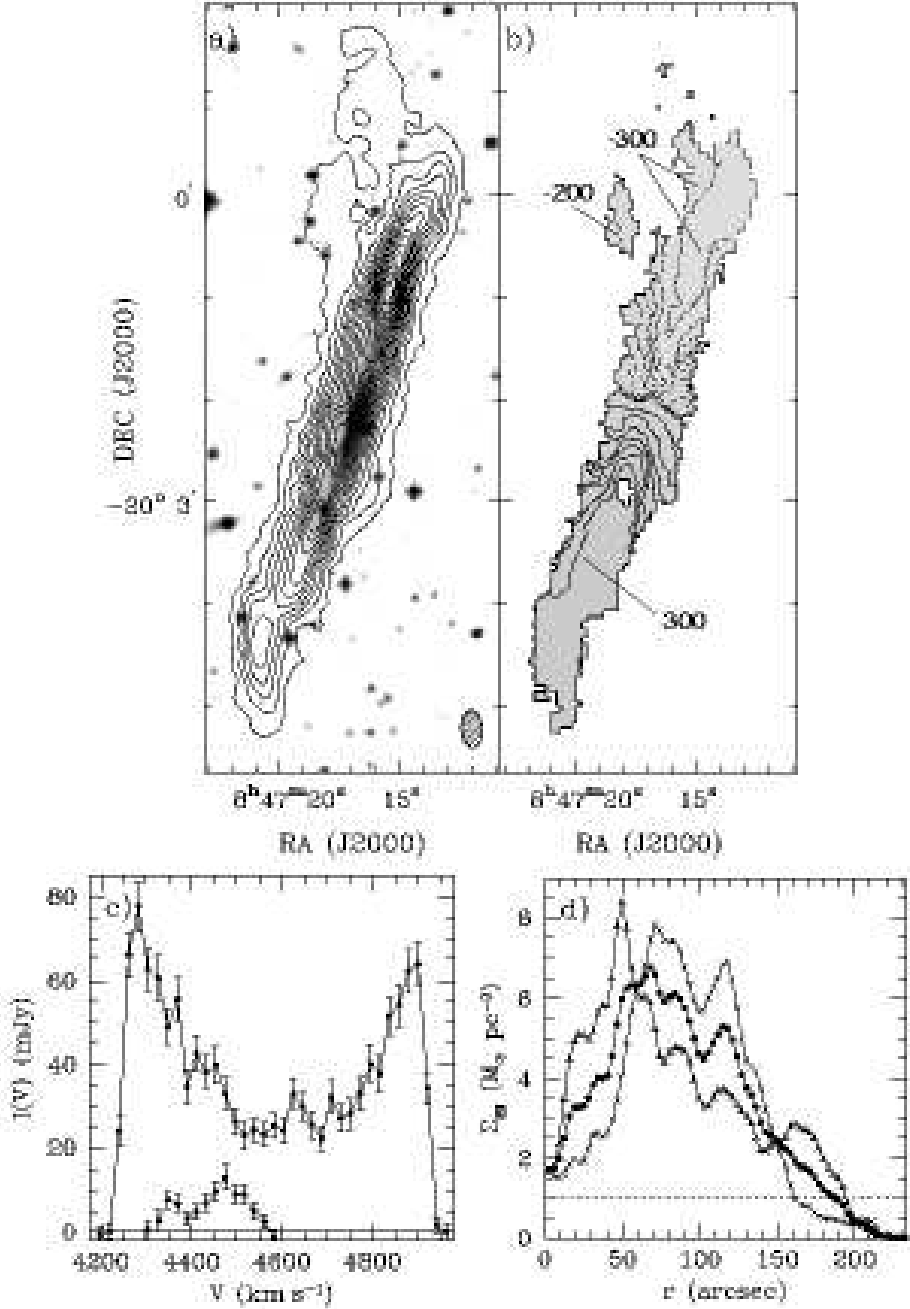


FIG. 4.— Same as in Fig. 2, but for ESO 563G21. In a), naturally weighted H I contours range from $3.4 \times 10^{20} \text{ cm}^{-2}$ to $1.8 \times 10^{22} \text{ cm}^{-2}$ in $1.1 \times 10^{21} \text{ cm}^{-2}$ intervals, overplotted on a DSS image.

problem was also noted by G04, who adjust the inner points of their RCs by hand. Since the RC gradients in the outer disks are small for the fast rotators (Figs. 11–12), and since beam smearing corrections are necessarily *ad-hoc* (e.g. Braun 1997; G04) and will further depress $V_{MET}(\alpha, \delta)$ in the inner regions, we apply no such corrections to the velocity fields. We note that H I points within the inner 1.5 beams of the galaxy center are ultimately dropped in the hybrid RC derivation (see §4.3); our neglect of this effect thus has no impact on the final results.

The application of the MET method to our data is demonstrated in Fig. 10. The crosses show $V_{MET}(r_i)$

along the peak of the intensity distribution, and the upper dashed horizontal line shows the value computed from the line profile in the right panel. At large r there is little low-velocity gas along the line of sight, and $V_{MET}(r_i) \simeq V_{mom1}(r_i)$. Within r_{opt} , it is clear that $V_{MET}(r_i)$ resembles the $V_{obs}(r_i)$ from optical spectroscopy (solid circles) much more closely than does $V_{mom1}(r_i)$ (triangles). In particular, there is good agreement between $V_{MET}(r)$ and $V_{obs}(r)$ measured in the optical near r_{opt} , leading to a smooth transition between the kinematics derived from the two tracers.

The MET velocity fields derived within the lowest contour in Figs 2a–9a are shown in Figs 2b–9b (shaded re-

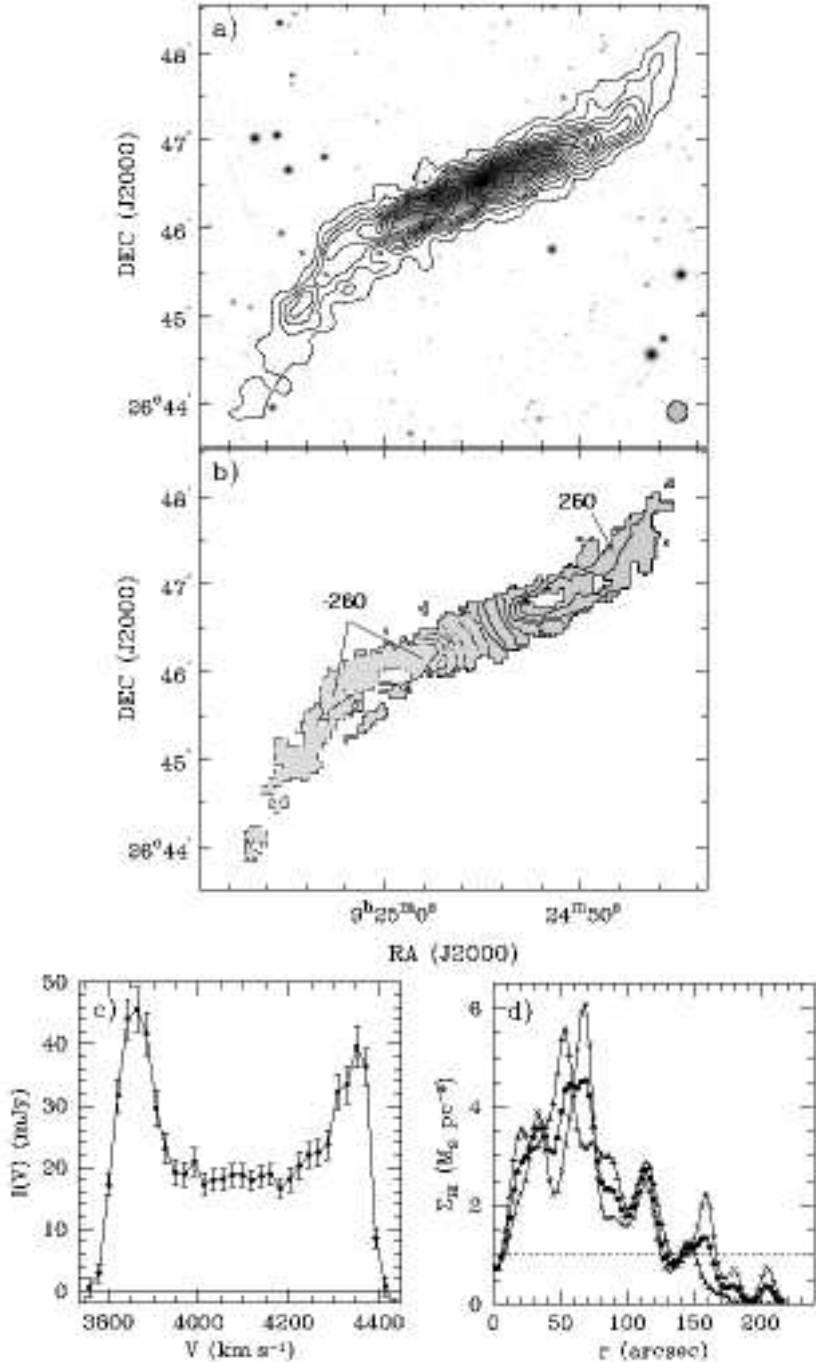


FIG. 5.— Same as in Fig. 2, but for NGC 2862. In a), H I contours range from $1.3 \times 10^{20} \text{ cm}^{-2}$ to $3.8 \times 10^{21} \text{ cm}^{-2}$ in $3.2 \times 10^{20} \text{ cm}^{-2}$ intervals, overplotted on an I -band image.

gions). The isovelocity contours are spaced at 40 km s^{-1} intervals: dotted lines denote the approaching side relative to V_{sys} in Table A6, and solid lines denote the receding side. Pixels within the H I disk with no V_{MET} estimates correspond to regions where a reliable gaussian fit to the extreme-velocity side of the profile could not be obtained. This is particularly prevalent near the galaxy centers, where beam smearing effects are large and the H I surface density is low (Figs 2d–9d).

We note that while the premise of the MET technique is physically motivated, the details of its application are

somewhat arbitrary. In particular, the fraction of the fitted gaussian peak adopted as $V_t(\alpha, \delta)$ and the form of the corrections applied are empirically derived (G04). In light of these uncertainties, Kregel & van der Kruit (2004b) argue that iterative least-squares modeling of PV diagrams yields superior disk kinematics to the method adopted here. However, the resolution and dynamic range in our data are insufficient to assure convergence of the technique, and it can only be applied along the major axes of edge-on galaxies; as such, we do not consider it here. Moreover, the excellent agreement between

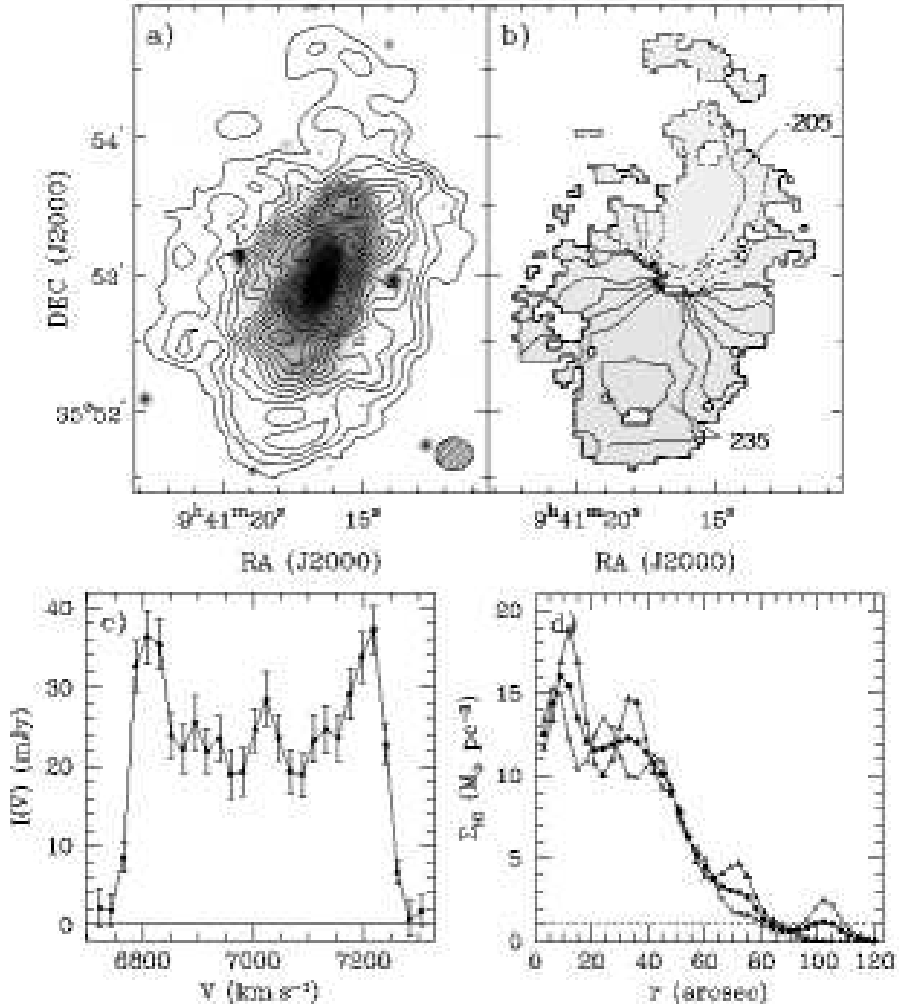


FIG. 6.— Same as in Fig. 2, but for NGC 2955. In a), H I contours range from $1.7 \times 10^{20} \text{ cm}^{-2}$ to $2.8 \times 10^{21} \text{ cm}^{-2}$ in $1.7 \times 10^{20} \text{ cm}^{-2}$ intervals, overplotted on a DSS image.

TABLE 5
H I PROPERTIES OF THE DETECTED COMPANIONS

Name (1)	Parent (2)	Separation (') (3)	$a \times b$ (' \times ') (4)	$\int Idv$ (Jy km s $^{-1}$) (5)	$W \sin i$ (km s $^{-1}$) (6)	V_{sys} (km s $^{-1}$) (7)	M_{HI} ($\times 10^9 M_\odot$) (8)	M_T ($\times 10^9 M_\odot$) (9)
HI034538+444639	UGC 2849	4.7	(S)	0.15×0.05	0.56 ± 0.07	119 ± 16	7897	1.7 ± 0.2
HI034553+445126	UGC 2849	3.5	(E)	0.11×0.06	0.7 ± 0.1	129 ± 7	8365	2.2 ± 0.3
ESO 563G22	ESO 563G21	5.9	(NE)	1.1×0.2	1.7 ± 0.2	173 ± 21	4429	2.0 ± 0.2
KUG 1634+392	NGC 6195	5.7	(N)	0.3×0.3	0.29 ± 0.05	42 ± 19	8975	1.2 ± 0.2
HI163617+390413	NGC 6195	4.0	(NW)	0.13×0.08	0.83 ± 0.07	99 ± 11	9085	3.3 ± 0.3
CGCG 341-027	UGC 11455	3.4	(NW)	0.55×0.2	0.78 ± 0.08	263 ± 18	5146	1.1 ± 0.1
^a No correction for inclination applied since $a = b$; lower limit.								

NOTE. — Col. (1): Source name. Optical identifications used where possible. For previously uncatalogued sources, names assigned from J2000 coordinates of H I centroid in total intensity maps. Col. (2): Parent galaxy. Col (3): Projected separation from parent galaxy. Direction of companion relative to parent is given in parentheses. Col. (4): Optical dimensions from literature if available, otherwise estimated from I -band (HI163617+390413) or DSS (HI034538+444639, HI034553+445126) images. Col. (5): Integrated line intensity. Col. (6): Velocity width at 50% of the peak, corrected for instrumental broadening. Col. (7): Integrated profile mid-point. Col.(8): H I mass, computed from eq. 2 using D for parent galaxy. Col. (9): Total dynamical mass, computed from eq. 3 (see text).

^aNo correction for inclination applied since $a = b$; lower limit.

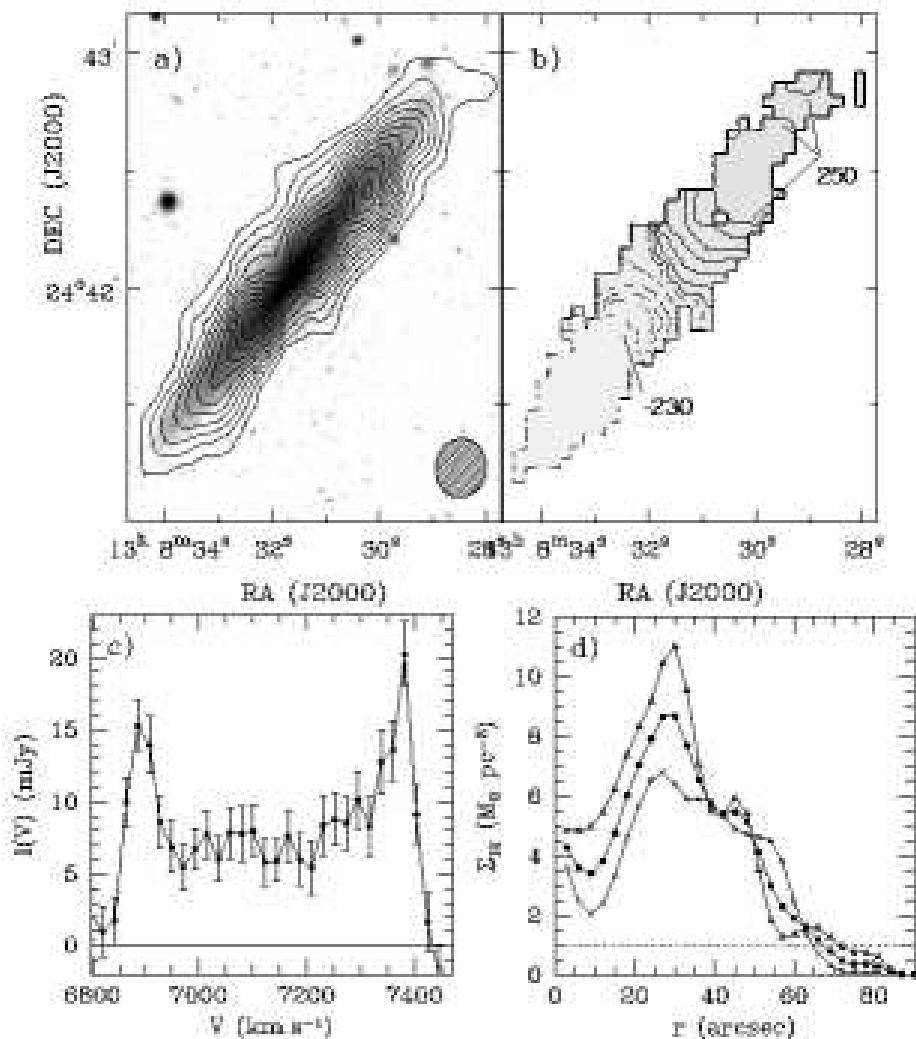


FIG. 7.— Same as in Fig. 2, but for IC 4202. In a), H I contours range from $4.0 \times 10^{20} \text{ cm}^{-2}$ to $4.0 \times 10^{21} \text{ cm}^{-2}$ in $3.3 \times 10^{20} \text{ cm}^{-2}$ intervals, overplotted on an *I*-band image.

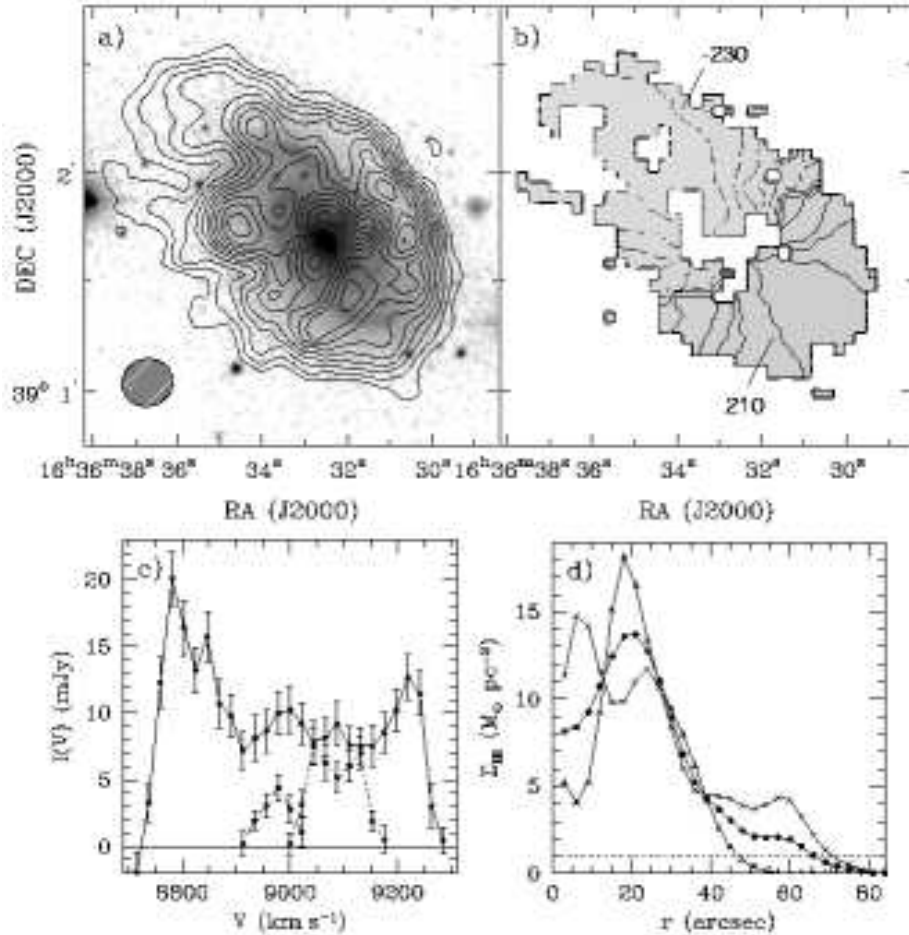


FIG. 8.— Same as in Fig. 2, but for NGC 6195. In *a*), H I contours range from $2.7 \times 10^{20} \text{ cm}^{-2}$ to $4.8 \times 10^{21} \text{ cm}^{-2}$ in $1.4 \times 10^{20} \text{ cm}^{-2}$ intervals, overplotted on an *I*-band image.

the optical and H I RCs at r_{opt} as well as that between the observed and simulated H I morphologies discussed in §4 suggest that the MET technique is indeed recovering $V_c(r) \sin i$, and that further refinements to eq. 5 are unnecessary.

4. RC DERIVATION

In this section we derive H I RCs from the velocity fields in Figs. 2b–9b, and combine them with the optical RCs of §2.2. We note that slightly different methods are adopted to obtain H I RCs the highly inclined and intermediate i systems in the sample, and we discuss each case in turn below. Since $i_d = 78^\circ$ for NGC 1324, its kinematics can be determined using either approach: we verify that both produce the same result. Because r_{pe} for NGC 1324 is similar to those of UGC 2849, NGC 2955 and NGC 6195 (Table 3), however, we group it with the intermediate i systems below.

4.1. H I RCs for the Highly Inclined Systems

We determine $V_{obs}(r)$ for the highly inclined systems ESO 563G21, NGC 2862, IC 4202 and UGC 11455 by averaging $V_{MET}(\alpha, \delta)$ from Figs. 2b–9b within a synthesized beam of the intensity distribution peak in Figs. 2a–9a. This strategy is similar to the Warped MET technique described by G04, and naturally fol-

lows the disk kinematics along the ridge of any warp that may be present in the disk. For ESO 563G21, NGC 2862 and UGC 11455 we estimate the warp parameters by tracing θ of the intensity distribution peak, as in García-Ruiz et al. (2002). We also adopt their definition of the warp angle α (their eq. 4) as that between the major axis and a line connecting the galaxy center and the outermost measured point in the warp. The derived α are accurate to $\sim 5^\circ$, while the warp radii r_w are accurate to a few kpc. The warp parameters for these systems are given in Table A6 (see also §A), and r_w is shown in Fig. 11.

To verify that the RCs, α and r_w derived are consistent with the H I morphologies of each system, we simulate observations of H I disks with the derived properties and compare them to the channel maps in Figs. 15c, 15d, 15f and 15h. Each galaxy is modeled by concentric rings with a user-supplied i , θ , V_c and Σ_{HI} . All rings have systemic velocities $V_o = V_{sys}$ from Table A6 and centers $(\alpha_o, \delta_o) = (\alpha_c, \delta_c)$ from Table 1. We model the approaching and receding sides of each fast rotator separately, setting $V_c(r_i) = V_{obs}(r_i)/\sin i$ and using $\Sigma_{HI}(r_i)$ from Figs. 2d–9d at the center r_i of each ring. We set $\theta = \theta_d$ for $r_i < r_w$, and for $r_i > r_w$ we introduce a smooth variation in θ consistent with α . We set $i = i_d$ at all r_i , and also adopt $\sigma_{ISM} = 10 \text{ km s}^{-1}$ as well as an exponential

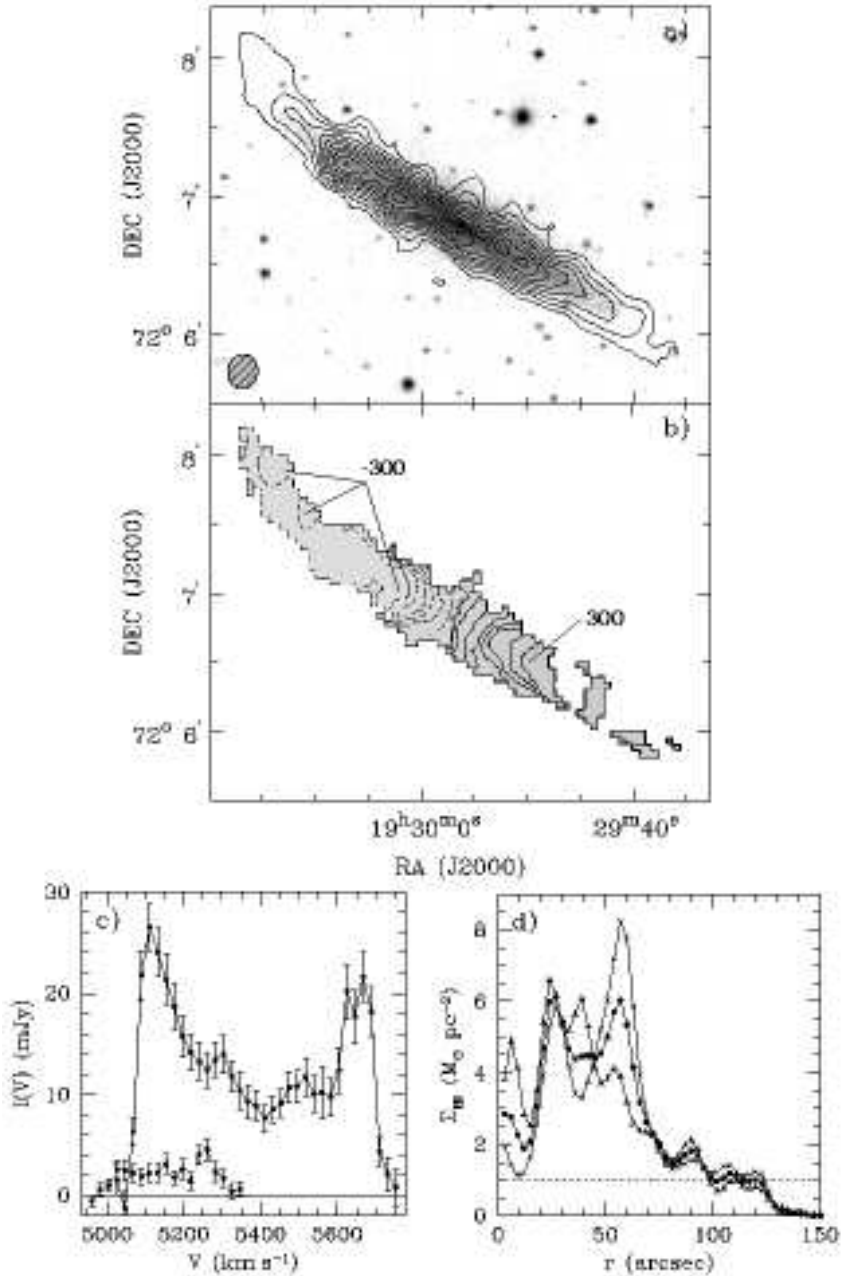


FIG. 9.— Same as in Fig. 2, but for UGC 11455. In a), H I contours range from 3.9×10^{20} cm $^{-2}$ to 4.5×10^{21} cm $^{-2}$ in 3.9×10^{20} cm $^{-2}$ intervals, overplotted on an I -band image.

H I scale-height of 1 kpc.

We find good agreement between the simulated data cubes and the channel maps in Figs. 15a–15h for all of the highly inclined systems. In particular, setting $i = i_d$ reproduces the observed H I morphologies even beyond r_w : i of the detected warps thus approaches that in the corresponding disk. We experiment with different input i beyond r_w , and find that setting $i \lesssim 80^\circ$ in the simulations fails to recover the H I channel maps in the warp regions. There is therefore no ambiguity between $V_{obs}(r)$ and i in these systems. Our simulations also demonstrate that the derived H I surface densities, kinematics and disk geometries for the highly inclined fast rotators self-consistently recover the morphology of the detected

emission.

4.2. H I RCs for the Intermediate i Systems

When H I disks at intermediate i are sufficiently resolved, RCs can be derived by fitting a series of concentric rings to the observed velocity field and by solving for V_c , V_o , i , θ and (α_o, δ_o) in each ring (Begeman 1989). We perform a tilted-ring analysis of the intermediate- i systems, first allowing all 6 parameters to vary and then fixing V_o and (α_o, δ_o) and re-fitting for V_c , i and θ . The values of V_o , (α_o, δ_o) and θ obtained from the fits are comparable to V_{sys} (Table A6), (α_c, δ_c) (Table 1) and θ_d (Table 2), respectively. However, the best fitting i are lower than i_d (Table 2) by an average of 15%, and $V_c(r)$ is

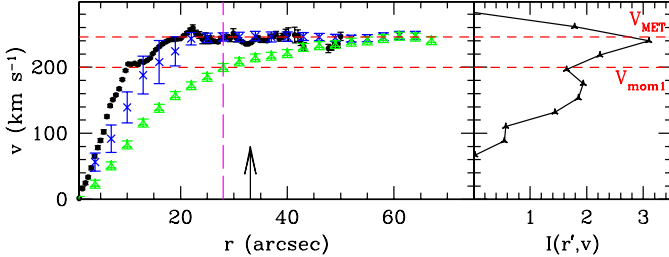


FIG. 10.—Left panel: comparison between $V_{mom1}(r_i)$ (triangles) and $V_{MET}(r_i)$ (crosses) for the receding side of IC 4202. The solid circles show the velocities derived from long-slit spectroscopy, for which beam smearing effects are negligible. The vertical long-dashed line shows the location r' at which $I(r', v)$ in the right panel is extracted (units are arbitrary), and the horizontal dashed lines show $V_{mom1}(r')$ (bottom) and $V_{MET}(r')$ (top). The solid arrow denotes r_{opt} . The MET technique mitigates the impact of beam smearing in the H I kinematics, and there is good agreement between $V_{MET}(r_i)$ and optical tracers near r_{opt} . A color version of this figure is available in the electronic edition of the Journal.

~10% larger than that from the optical kinematics and from major-axis slices. In addition, simulated datacubes of systems with these properties produce models with spatial and spectral extents that are too large when compared to observations. These discrepancies arise from the low angular resolution of the latter along the minor axes of the intermediate- i systems (Figs. 2a–9a): beam smearing blends major axis gas with lower velocity off-axis material in this direction, and broadens the spatial extent of the emission. This leads to an underestimate of i and a corresponding overestimate of V_c in the tilted ring models. The biases on the ring properties are analogous to those encountered when ellipse fits are used to determine $\Sigma_{HI}(r)$ (see §3).

We therefore derive the RCs for NGC 1324, UGC 2849, NGC 2955 and NGC 6195 in a manner similar to that for the high i systems, averaging $V_{MET}(\alpha, \delta)$ from Figs. 2b–9b in a slice the width of a synthesized beam oriented at θ_d (Table 2). We thus implicitly assume that the major axis of the H I disk lies within a beam of the I -band major axis. These assumptions do appear to be justified given the H I morphologies and kinematics in Figs 2–9.

To verify the plausibility of the $V_{obs}(r)$ obtained, we simulate observations of each intermediate i fast rotator in a similar manner as for the highly inclined systems. We model the approaching and receding sides of each galaxy separately, adopting $\Sigma_{HI}(r)$ from Figs. 2d–9d and $\theta = \theta_d$ at all r . Unlike the near edge-on case, however, at intermediate i there is an ambiguity between i and the RC amplitude in the outer H I layer. In our sample, $V_{obs}(r)$ for NGC 1324, UGC 2849 and NGC 2862 declines beyond r_{opt} on at least one side (see §4.3). Moreover, changes in i of only a few degrees have a significant impact on the resulting $V_c(r) = V_{obs}(r)/\sin i$: these decreases may thus represent a change in the gravitational potential in these regions, or may result from variations in the disk geometry. Note that minor axis distortions indicative of a warped disk are difficult to detect in our data, due to limited spatial resolution along this axis: we therefore make no attempt to measure warp parameters in the intermediate i systems.

To investigate the extent to which the H I channel maps resolve this ambiguity, we construct two models

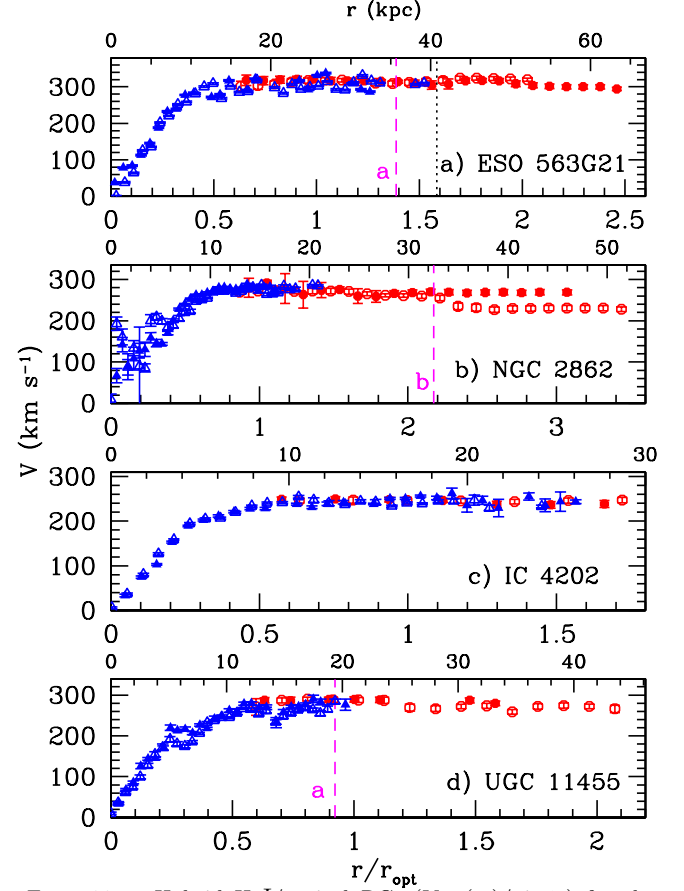


FIG. 11.—Hybrid H I/optical RCs ($V_{obs}(r_i)/\sin i_d$) for the highly inclined galaxies. In each panel, r_i is in units of r_{opt} on the lower horizontal axis, and in kpc on the upper horizontal axis. RC points derived from long-slit spectroscopy are denoted by triangles, and those from the H I observations are denoted by circles. Empty symbols correspond to the approaching side, and filled symbols to the receding side. The dashed vertical lines indicate the measured warp radii, and the label to the lower left of each line distinguishes warps on the approaching (a), receding (r), or both (b) sides of the disk. The galaxy name is given in the bottom right corner. For ESO 563G21 in a), the dotted vertical line shows the approximate starting location of the SE feature; see §A.3. A color version of this figure is available in the electronic edition of the Journal.

for each of the galaxies with declining $V_{obs}(r)$. In the first model we set $i = i_d$ at all r , and in the second we introduce a smooth decrease (increase for the approaching side of UGC 2849) in i beyond r_{opt} to produce a flat RC. Details of this second model are given in the notes in §A, but $0^\circ < i_d - i(r_{HI}) < 15^\circ$ for all systems. In general, there is good agreement between the simulated observations and the measured channel maps for both models (see §A for details): the available data thus cannot distinguish between a falling RC due to a change in the gravitational potential beyond r_{opt} or one caused by a variation in i associated with a warp. We discuss this further in §5.

4.3. Hybrid RC Derivation

Further processing of the H I RCs as well as their combination with the optical RCs discussed in §2.2 is done homogeneously for all of the sample galaxies. We fold each H I RC about the point (r_{min}, V_{min}) that minimizes the difference between the approaching and re-

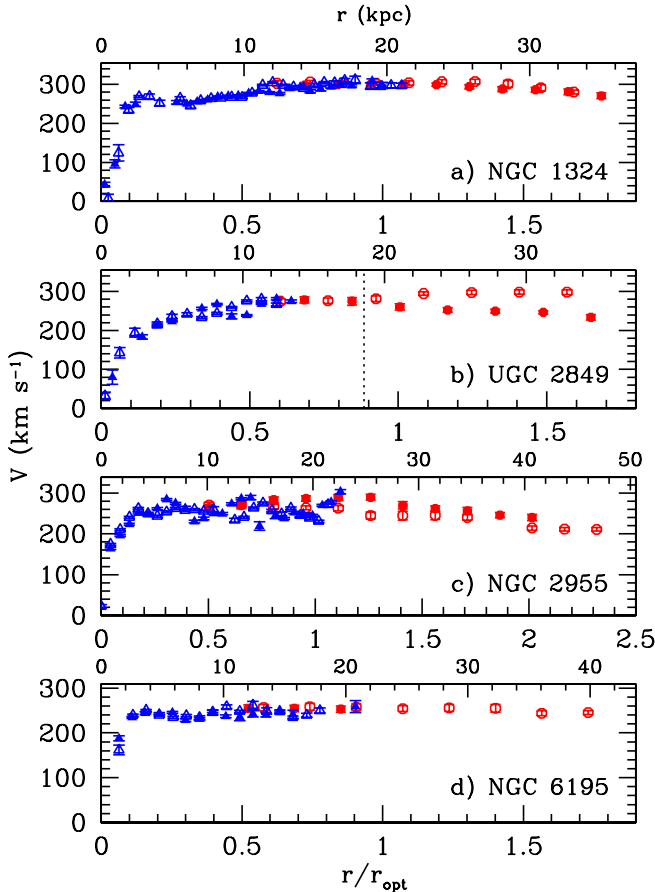


FIG. 12.— Hybrid H I/optical RCs ($V_{obs}(r_i)/\sin i_d$) for the intermediate i galaxies; plot details are the same as in Fig. 11. For UGC 2849 in b), the dotted vertical line shows the approximate starting location of the H I emission on the receding that may be associated with interactions between this galaxy and the detected companions; see §A.2. A color version of this figure is available in the electronic edition of the Journal.

ceding sides within r_{opt} . These points are assigned to $r = 0, V = 0$ in the RC, and they differ by no more than 15 km s^{-1} and $5''$ from V_{sys} measured in §3.1.1 (Table A6) and the optical center (α_c, δ_c) (Table 1), respectively. We assign half the difference between $V_{MET}(r)$ obtained when $V_i(\alpha, \delta)$ in eq. 5 is measured at 50% of the $I(\alpha, \delta, v)$ peak and when it is measured at 20% of the peak as the error on each H I RC point. The H I RCs are then resampled to $6''$ ($6.2''$ for ESO 563G21), yielding slightly less than 2 points per synthesized beam.

We then combine the optical and H I RCs, dropping H I points within 1.5 synthesized beam widths of $r = 0$ to avoid beam smearing biases on $V_{obs}(r)$ (§3.1.2) and correcting r_i of the remaining H I points for beam smearing. We also clip optical RC points that are discrepant by over 50 km s^{-1} , and thus likely the result of non-circular motions or patchy emission regions in the disk. Finally, we correct for galaxy geometry using i_d from Table 2. This has a negligible effect on the kinematics of the highly inclined systems, but the RC amplitudes and shapes in the intermediate i subsample depend on this choice.

The hybrid H I/optical RCs ($V_{obs}(r_i)/\sin i_d$) for the highly inclined galaxies in the fast rotator sample are shown in Fig. 11, and those for the intermediate i systems are in Fig. 12. In each panel, the triangles denote

points derived from long-slit spectra while the circles denote points obtained from H I observations. Empty and filled symbols show the approaching and receding sides, respectively. In Fig. 11 dashed lines indicate r_w in the highly inclined systems with warps, and those on the approaching (a), receding (r) or both (b) sides of the disks are labeled to the lower left of the line. For ESO 563G21 in Fig. 11a, the dotted line shows the approximate starting location of the SE feature; see §A.3 for details. Beyond the vertical dotted line in Fig. 12b, the H I channel maps on the receding side of UGC 2849 are not well modeled by either a co-planar or warped disk; it is possible that interactions with its detected companions are distorting the H I layer in this region (see §A.2).

For all of the sample galaxies, there is a smooth transition between the optical and H I RCs as well as excellent agreement between points in the overlap regions near r_{opt} . This suggests that the ionized and atomic components of the interstellar medium (ISM) have similar geometries at this location in the underlying galaxy potential.

5. DISCUSSION AND SUMMARY

We have presented I -band photometry, long-slit optical spectra, and new H I aperture synthesis observations for 8 rapidly rotating nearby spirals. Despite their large scales, the sample galaxies lie on the size, velocity, absolute magnitude and surface brightness scaling relations in the SFI++ database, and their global gas fractions and surface densities are within the ranges expected for their morphological types (§3.1.1; Table A6). These “fast rotators” thus represent the high-mass extreme of the normal, late-type spiral galaxy population. We derive hybrid optical/H I rotation curves (RCs) for each system, and find a good correspondence between the H I rotation velocities derived using G04’s Modified Envelope Tracing method and those from optical spectra in regions probed by both tracers (Figs. 11–12). In a forthcoming paper we will mass model the kinematics presented here, and estimate corresponding angular momentum distributions as well as spin parameters λ for a range of baryon mass-to-light ratios (Spekkens & Giovanelli 2006, in preparation).

In general, the detected H I emission in each galaxy has the morphology of a thin rotating disk with the same geometry as its I -band stellar distribution. However, we find that warps are prevalent beyond r_{opt} in massive spirals: all of the highly inclined, extended H I disks that we detect are warped on one or both sides, and the channel maps for the intermediate inclination (i) systems are also consistent with warped outer layers. Some of these warps (e.g. ESO 563G21, UGC 11455) may be excited by companions, which we detect in the vicinity of half the sample galaxies (Table 5). Interactions with these smaller systems may have also produced the H I features in UGC 2849 (Fig. 12; §A.2) and ESO 563G21 (Fig. 11; §A.3) that we are unable to recover in our disk models of the observed H I emission. As a counter-example, however, we point out the spectacular symmetric warp in the *isolated* system NGC 2862 (Figs. 5, 15d): its warp angles are comparable to the largest detected by García-Ruiz et al. (2002) in their sample of 26 edge-on spirals, and are 30% larger than those in their isolated systems.

Despite the presence of warps and other features in

the H I morphologies of the fast rotators, their kinematics are very regular. ESO 563G21 is an extreme example: we detect prominent H I extensions on either end of the major axis (Fig. 4), but find well-ordered rotation throughout the H I layer irrespective of the inclusion of the discrepant emission (§A.3; Fig. 11a). There is also excellent agreement between the kinematics of the approaching and receding sides in most systems (exceptions are UGC 2849 for $r > r_{opt}$ and NGC 2862 for $r > 2.2r_{opt}$), as well as $V_{obs}(r)$ determined from H I and optical spectroscopy in the overlap region near r_{opt} . The symmetry and regularity in the inferred dynamics reflects the depth of the gravipotential wells and the similar geometries of the ionized and atomic ISM components in these massive systems. For all sample galaxies except IC 4202, the H I RCs extend well beyond those in the optical, probing the structure of the fast rotators out to $1.7r_{opt} \lesssim r \lesssim 3.5r_{opt}$.

The derived RCs are very flat beyond r_{opt} . This is particularly the case for the highly inclined systems, where $V_{obs}(r) \simeq V_{rot}$ and projection effects are negligible. With the exception of the warp region on the approaching side of NGC 2862, $V_{obs}(r) \simeq$ Constant at $r \gtrsim 0.5r_{opt}$ for all RCs in Fig. 11. For galaxies at intermediate i , there is an ambiguity between i and the derived RC amplitude (§4.2). In particular, the outer RCs for NGC 1324 (Fig. 12a) and NGC 2955 (Fig. 12c) decline on both sides when the stellar disk i_d is adopted to correct for disk geometry beyond r_{opt} . NGC 2955 exhibits the strongest outer RC gradient in the sample, decreasing steadily beyond r_{opt} to $V_{obs}(r_{HI})/\sin i_d \sim 0.75V_{rot}$. However, the H I channel maps of the intermediate i systems are consistent with *both* the RCs of Fig. 12 and flat RCs with decreasing (increasing for the approaching side of UGC 2849) i to mimic a warp. In addition, NGC 2955 has the lowest i_d in the fast rotator sample, and a gradient $\Delta i \lesssim 1^\circ \text{kpc}^{-1}$ is sufficient to reconcile the declining $V_{obs}(r)/\sin i_d$ of Fig. 12c with a flat RC beyond r_{opt} . Because of the shallow derivative of the sine function near $\sin i \sim 90^\circ$, a gradient of this amplitude is not detectable in the outer H I layers of our near edge-on systems. Indeed, since we obtain flat RCs for the highly inclined sample galaxies where i effects are negligible, and since intrinsic galaxy properties should not correlate with viewing geometry, it seems likely that the falling RCs of the intermediate i fast rotators are the result of warps rather than changes in the gravipotential wells of these systems. This suggests that *all* of the massive galaxies studied here have flat RCs.

We quantify the outer RC shapes discussed above by computing the logarithmic slope $S = d \log(V_{obs}(r)/\sin i_d)/d \log r$ for each system. We adopt the definition of CvG91, and measure S from the best fitting linear trend to the RC between $2/3r_{235}^o$ and the outermost RC point, where r_{235}^o is the radius of the 23.5th mag asec^{-2} I -band isophote corrected to a face-on perspective (Table 2; r_{235}^o in I -band is roughly equivalent to D_{25} in B -band). We measure the slopes for the approaching and receding sides of each RC separately, and compute their average weighted by the RC extent on each side to produce S . The values obtained are given in Table 3, and are plotted in Figs. 13 and 14.

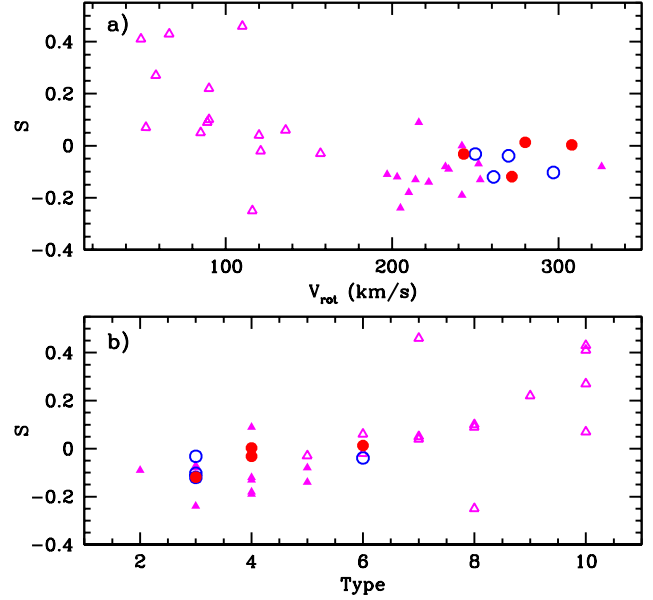


FIG. 13.— Logarithmic outer slope S as a function of a) V_{rot} , b) morphological type. In both panels, solid circles show the highly inclined galaxies in the present sample, and empty circles show those at intermediate i . Note that at high i , there is no ambiguity between S and i . For the intermediate i galaxies, S is computed using i_d from Table 2. Triangles show the sample of H I RCs collected by Casertano & van Gorkom (1991, hereafter CvG91): open symbols show systems with $V_{rot} < 180 \text{ km s}^{-1}$, and solid symbols show systems with $V_{rot} > 180 \text{ km s}^{-1}$. S decreases with increasing V_{rot} for $V_{rot} \lesssim 220 \text{ km s}^{-1}$, in accordance with the trend noted by CvG91; however, it plateaus in higher mass systems. The trend between S and morphological type for the high-mass systems ($2 \leq \text{type} \leq 6$) is also considerably weakened when both samples are considered. A color version of this figure is available in the electronic edition of the Journal.

The solid circles in Figs. 13 and 14 show S for the highly inclined fast rotators, and open circles correspond to the intermediate i fast rotators. The triangles show the sample of galaxies with extended RCs compiled by CvG91 (their table 2): open triangles are systems with $V_{rot} < 180 \text{ km s}^{-1}$ (Fig. 13), and solid triangles are systems with $V_{rot} > 180 \text{ km s}^{-1}$ (Figs. 13 and 14). Note that CvG91 compile B -band photometry for their sample galaxies, while ours is in the I -band. We ignore this difference in Fig. 14a, since variations in r_d measured in the two bands are comparable to the uncertainties on these parameters (e.g. de Jong 1996). For ease of comparison with fig. 7 of CvG91, we use $H_o = 75 \text{ km s}^{-1} \text{ Mpc}^{-1}$ to convert r_d^o to physical scales for the fast rotators in Fig. 14a. In Fig. 14b, we adjust $\mu_{e,I}$ from Table 2 using $B - I$ colors estimated from our data and B_T^0 from the RC3 where available (de Vaucouleurs et al. 1991), or else we adopt $B - I = 1.8$ (the mean for the fast rotators with B_T^0 estimates). Figs. 13 and 14 are thus analogous to figs. 6–9 of CvG91 with the fast rotator points overplotted, though the comparisons of Fig. 13 are more reliable than those in Fig. 14 given the different photometric bands used in the latter.

Figs. 13 and 14 demonstrate that the outer RC shapes for the fast rotator sample are flatter than expected from the trends in CvG91. This is most obvious in Fig. 13a,

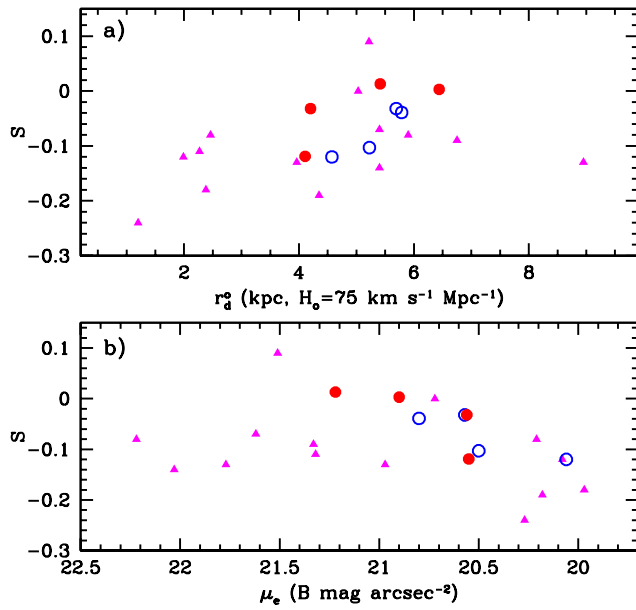


FIG. 14.— Logarithmic outer slope S as a function of a) r_d^o (computed from $H_o = 75 \text{ km s}^{-1} \text{ Mpc}^{-1}$, as in CvG91), b) μ_e . Plot details are the same as in Fig. 13. Note that CvG91 use B -band photometry in their analysis, while ours is in I -band: we ignore this difference in a). In b), we adjust $\mu_{e,I}$ from Table 2 using $B - I$ colors derived from our data and B^T from the RC3 where available, or else adopting $B - I = 1.8$. There is some evidence that galaxies with larger r_d^o have larger S , but the trend depends strongly on the inclusion of outliers in S and r_d^o . There is no clear correlation between S and μ_e for massive spirals when the CvG91 and fast rotator samples are combined. A color version of this figure is available in the electronic edition of the Journal.

where S plateaus for $V_{rot} \gtrsim 220 \text{ km s}^{-1}$ for *both* members of the present sample and for those in the CvG91 compilation: the anti-correlation between S and V_{rot} noted by CvG91 thus does not extend to the high-mass end of the spiral galaxy population. Fig. 13b also shows that the correlation between S and morphological type for the high-mass systems is weakened when both samples are considered. The correlation between r_d^o and S (Fig. 14a) noted by CvG91 remains, though the trend is dominated by a few outliers in S and r_d^o . However, there is no clear correlation between S and μ_e (Fig. 14b) when the fast rotators and the massive systems from CvG91 are combined. We remind the reader, however, that the comparisons in Fig. 14 are muddled by the different photometric bands employed here and in CvG91: an updated compilation of high-surface brightness galaxies with reliable extended RCs and homogeneous photometry would better address this issue.

We note again here that there is an ambiguity between i and S for the intermediate i fast rotators. We have adopted i_d to compute S here, and from the arguments above the open circles in Figs. 13 and 14 are likely underestimates of the true S in these systems. Shifting these points towards $S = 0$ in each panel do not change the above conclusions. We have also verified that varying the region in the outer RC used to compute S has little impact on our results.

To summarize, the kinematics of the fast rotators im-

ply that the RCs of massive, late-type spirals are flat and featureless for $r \gtrsim 0.5 r_{opt}$ out to their last measured RC points, the latter in the range $1.7 - 3.5 r_{opt}$. We thus find no convincing evidence that massive late-type galaxies have declining RCs, nor that their outer RC slopes correlate well with morphological type, scale-length or central surface brightness. If the inner regions of massive disk galaxies are baryon-dominated, the transition to dark matter domination beyond r_{opt} leaves no imprint on the resulting kinematics. The disks and halos of rapidly rotating spirals thus appear to “conspire” just as effectively as those in lower mass systems.

Many thanks to M. P. Haynes for assistance with the SFI++ I -band images and photometry, to L. van Zee for advice regarding H I rotation curve derivations and to G. Gentile for help in implementing the MET method. We are also grateful to B. Catinella, C. Valotto and N. P. Vogt for obtaining and reducing the long-slit optical spectra, as well as to the many members of our group who acquired and reduced I -band images over multiple observing runs. Thoughtful comments from the referee also helped improve the clarity of the text. This research has made use of the NASA/IPAC Extragalactic Database (NED) which is operated by the Jet Propulsion Laboratory, California Institute of Technology, under contract with the National Aeronautics and Space Administration. This research was partially funded by National Science Foundation grants AST-0307396 and AST-0307661.

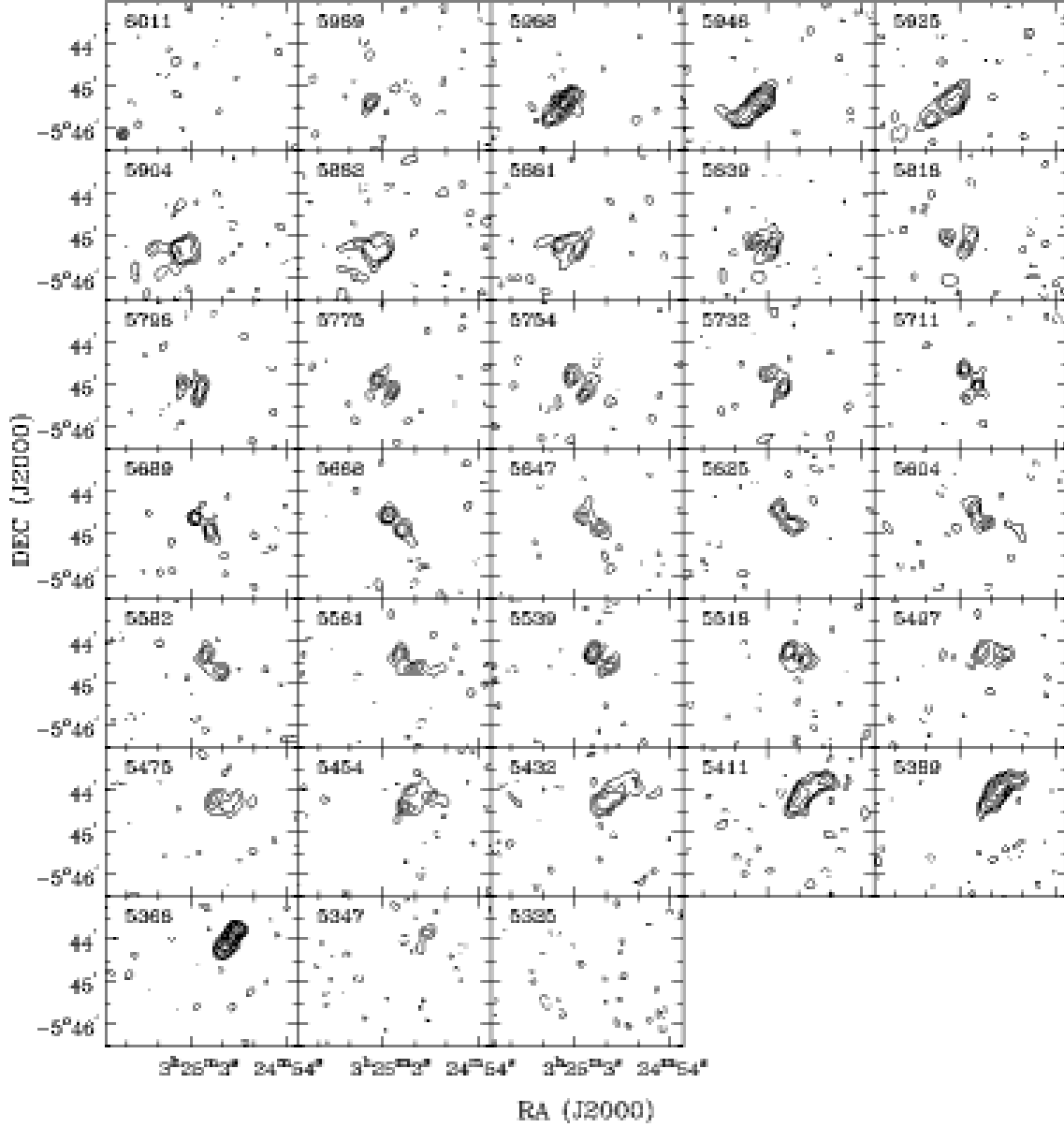


FIG. 15A.— Uniformly weighted channel maps for NGC 1324. Contours are at $0.45 \times (-3.5, -2, 2 (2\sigma), 3.5, 5, 8, 11, 14, 16)$ mJy/beam. In each panel, the heliocentric (optical) radial velocity is in the upper left corner. The synthesized beam is in the lower left corner of the first panel. Figures 15b–15h are available in the electronic edition of the Journal.

APPENDIX

CHANNEL MAPS AND NOTES ON INDIVIDUAL SYSTEMS

In this appendix we present channel maps of the H I emission for each of the sample galaxies as well as notes on individual systems. The channel maps are given in Figs. 15a–15h. All of the maps are corrected for primary beam attenuation, and the weighting adopted is the same as that used in the analysis of §3.1.1. For ESO 563G21, NGC 2862 and UGC 11455, we plot a subset of the channels near the datacube center for conciseness; otherwise, we plot the data at full spectral resolution.

NGC 1324

NGC 1324 is a field spiral with prominent spiral structure (Fig. 2a): there is a high degree of symmetry in the optical image, and no hint of a bar. The *I*-band photometry of Paturel et al. (2003a) is in good agreement with the values listed in Table 2. In their compilation of bulge statistics from DSS imaging, Lüttingke et al. (2000b) find a bulge shape intermediate to a boxy profile and an elliptical. Both Giuricin et al. (2000) and Prada et al. (2003) classify NGC 1324

as the dominant member of a galaxy pair: however, Giuricin et al. group it with the spiral KUG 0325-053 nearly a degree away, while Prada et al. identify a small companion 15' away. This first of these putative companions lies well outside the primary beam of our VLA observations, while the second lies at its FWHM: we are not sensitive to either. A cursory search of the HI datacubes does not reveal any other companions in the vicinity of NGC 1324.

The channel maps for NGC 1324 in Fig 15a as well as the global properties presented in Fig. 2 are similar on the approaching and receding sides of the disk: the high degree of symmetry in H I and in the optical suggests that NGC 1324 is not interacting strongly with its neighbors. Our values of $\int Idv$, $W \sin i$, V_{sys} and M_{HI} for this system (Table A6) are in good agreement with published single-dish data (Theureau et al. 1998; Paturel et al. 2003b).

There is also good agreement between the H I and optical kinematics in NGC 1324 (Fig. 12a). A turnover in the HI RC beyond $r \sim 67''$ (~ 30 kpc) is detected on both sides, and $V_{obs}(r)/\sin i_d$ decreases by ~ 30 km s $^{-1}$ over ~ 8 kpc. The turnover may signal a change in the galaxy potential in this region, but is also consistent with a decrease in i from 78° to 62° and a flat RC. We construct galaxy models with both characteristics and compare them to the observed channel maps. In both cases the models recover the distribution of H I, though in each a change in position angle $\Delta\theta \sim 20^\circ$ beyond $r \sim 65''$ is required to reproduce the emission from 5946 – 5925 km s $^{-1}$ and from 5432 – 5389 km s $^{-1}$. The kinematics of NGC 1324 are therefore consistent with a warp for $r \gtrsim 30$ kpc, accompanied either by a falling RC or a systematic decrease in i .

UGC 2849

UGC 2849 is an intermediate i field galaxy with a regular morphology in DSS and 2MASS images. Little else other than single-dish H I observations of UGC 2849 are available in the literature.

In the channel maps for UGC 2849 in Fig. 15b the S/N of the H I emission is low in the channels near $V_{sys} = 8104$ km s $^{-1}$, particularly at small r where $\Sigma_{HI}(r)$ drops to $1 M_\odot$ pc $^{-2}$ (Fig. 3d). The morphology of the H I distribution is similar for the approaching and receding sides within r_{opt} , though there are significant differences farther out (see below). The H I is more extended on the west (W) side of the galaxy, due largely to a feature at 7866 km s $^{-1}$. Both the shape of the global profile and our estimates of $\int Idv$, $W \sin i$, V_{sys} and M_{HI} (Table A6) are in excellent agreement with the single dish data of Paturel et al. (2003b; see also Bottinelli et al. 1990).

We detect two companions to UGC 2849, 3.5' (~ 120 kpc in projection) and 4.7' (~ 150 kpc in projection) to the east (E) and south (S) of the main disk, respectively. There are no previously cataloged objects within 4.5' of either source: these systems represent new detections. The companions are only marginally resolved spatially, but channel maps (not shown) suggest that the S parts of both galaxies are advancing and the N parts are receding. Despite our relatively low spectral resolution, their global profiles show double peaks characteristic of inclined disks (Fig. 3c): this is corroborated by the axial ratios of candidate optical counterparts that we identify on DSS images. In addition, θ for the optical counterparts are roughly consistent with that expected from their H I morphologies. The properties of the two companions are given in Table 5. Note that their values of M_{HI} and M_T resemble those of the Local Group spiral M33, that has $M_{HI} = 1.8 \times 10^9 M_\odot$ and $M_T \sim 6 \times 10^9 M_\odot$ (Corbelli & Salucci 2000).

Though the optical RC is rising at the last measured point for UGC 2849, the H I RC is flat for 12 kpc $\lesssim r \lesssim 20$ kpc, and there is good agreement between the optical and H I velocities in the overlap region. There is, however, a significant discrepancy between $V_{obs}(r)/\sin i_d$ on the approaching and receding sides beyond r_{opt} : the approaching side rises to ~ 300 km s $^{-1}$ just beyond r_{opt} , but there is a smooth decrease on the receding side of ~ 2 km s $^{-1}$ kpc. If these deviations from a flat RC are caused by warping in the outer H I layer, we require i to increase from $i_d = 66^\circ$ to $i \sim 71^\circ$ on the approaching side beyond r_{opt} , and i to decrease systematically from $i_d = 66^\circ$ to $i \sim 50^\circ$ at the last measured H I point on the receding side. We model both sides of UGC 2849 separately, using $V_{obs}(r)$, $\Sigma_{HI}(r)$ and θ_d as inputs. On the approaching side, simulations where $i = i_d$ and ones where i increases to 71° beyond r_{opt} both reproduce the channel map morphology in Fig. 15b. Similarly, we construct two models of the receding side: the first adopts i_d throughout, and in the second i decreases as described to produce a flat RC beyond r_{opt} . Both simulations reproduce the observed H I morphologies from 8408 – 8365 km s $^{-1}$ in the channel maps of Fig. 15b, the first yielding a better match at 8365 km s $^{-1}$. However, neither model adequately recovers the broad, featureless emission from 8343 – 8300 km s $^{-1}$.

In summary, the derived RC for UGC 2849 shows unusual behavior beyond r_{opt} ; the dotted vertical line in Fig. 12b shows the approximate starting point of the pathologies. While we cannot distinguish between an asymmetric warp or distorted outer halo, tidal interactions between UGC 2849 and its nearby, M33-like companions are the likely culprit. Deep imaging or H I spectroscopy of the companions to look for irregular morphologies would confirm this hypothesis.

ESO 563G21

ESO 563G21 is a large, highly inclined galaxy in the southern sky included in the Flat Galaxy Catalog of Karachentsev et al. (1993, 1999). The I -band photometry of Paturel et al. (2003a) agrees well with the values listed in Table 2. Using DSS images, Lüttsche et al. (2000b) find an elliptical bulge in ESO 563G21, and Sánchez-Saavedra et al. (2003) detect a mild clockwise warp on both sides of the disk.

Because of its proximity and size, ESO 563G21 is among the best resolved galaxies in the sample. The channel maps in Fig. 15c show two distinct features at either end of the main disk: one from $4921 - 4836 \text{ km s}^{-1}$ at $\sim 8^h 47^m 21^s, -20^\circ 3' 30''$, and one from $4389 - 4262 \text{ km s}^{-1}$ at $\sim 8^h 47^m 17^s, -19^\circ 59' 30''$. Both features are detected over multiple channels in our data, and are evident in the total H I intensity map in Fig. 4a. The SE extension is compact, H I bright, and located well beyond r_{opt} on the receding side of the disk. Qualitatively, it appears morphologically distinct from the disk emission but not kinematically different from it. The approximate starting point of the SE feature is indicated by a dotted vertical line in Fig 11a. If associated with warp in the disk, its curvature is opposite that detected in the optical. The NE feature is faint and diffuse, and is both morphologically and kinematically distinct from the underlying disk emission. Extraplanar emission in the vicinity of this feature is detected over 10 frequency channels yielding a characteristic width of more than 200 km s^{-1} , and at the sensitivity of our data it extends up to 27 kpc (in projection) above the midplane.

We confirm that the spiral ESO 563G22 is a companion to ESO 563G21, with a projected separation of $5.9' (\sim 120 \text{ kpc})$ to the NE of the latter. ESO 563G22 is a highly inclined spiral with a disturbed optical morphology, and 2MASS data reveals an asymmetry with more emission in the N. We resolve the H I emission of ESO 563G22 only marginally, but the S part of the disk is receding and the N part is advancing. Its basic properties are given in Table 5. While M_{HI} for ESO 563G22 is comparable to that of M33, M_T exceeds that of the Local Group spiral by a factor of 5 (Corbelli & Salucci 2000). The orientation of the NE feature of ESO 563G21 lies roughly along the line joining it and ESO 563G22, indicating that it may be the result of an interaction between the two systems.

Despite the unusual H I morphology of ESO 563G21 (Fig. 4a) and significant differences between $\Sigma_{HI}(r)$ for the approaching and receding sides (Fig. 4d), both the global profile in Fig. 4c and the derived RC in Fig. 11a are symmetric. We find no difference between the RC derived including the NE and SE features and one derived excluding them, save for their extent on the receding side. We therefore include emission from these features in the parameters given in Table A6 and in the RC of Fig. 11. Our estimate of $\int Idv$ is intermediate to single dish values from Haynes et al. (1999b) and Paturel et al. (2003b), and the global properties V_{sys} and $W \sin i$ are in good agreement with published measurements.

Following the peak in the H I intensity distribution in Fig. 4a in the manner described by García-Ruiz et al. (2002), we measure a warp angle $\alpha = 6^\circ$ on the approaching side of ESO 563G21. The approximate starting point r_w of the warp is denoted by the dashed line in Fig. 11a. Our model of the ESO 563G21 datacube using $V_{obs}(r)$ and $\Sigma_{HI}(r)$ recovers the H I channel maps in Fig. 15c if i_d and θ_d are adopted throughout. These simulations do not reproduce the SE and NE features discussed above, however, and changes in i and θ at large r do not reconcile our models and the data in these regions. We note that the RC on the approaching side and that on the receding side within the dotted line in Fig. 11a are unchanged when the H I emission from the features is blanked from the datacubes.

NGC 2862

NGC 2862 is one of few massive isolated spirals with $cz \leq 5000 \text{ km s}^{-1}$ (Karachentseva 1973; Varela et al. 2004). We perform a cursory search for H I-rich companions in our data that may have been missed in optical surveys, and find none. Despite its classification as an unbarred system, a strong edge-on bar is identified by Lüticke et al. (2000a) from near-IR surface brightness distributions. This is corroborated by large deviations from circular motion at small r in the optical RC (Fig. 11b).

The H I channel maps for NGC 2862 in Fig 15d reveal a spectacular symmetric warp. The warp on the SE side of the galaxy extends farther than that on the NE side, with emission detected up to 40 kpc away from the mid-plane at 3864 km s^{-1} . Following the peak of the intensity distribution in Fig 5a and adopting the definition of the warp angle α of García-Ruiz et al. (2002), we measure $\alpha = 23^\circ$ and $\alpha = 19^\circ$ on the approaching and receding sides respectively. These are extreme relative to those in the 26 edge-on systems surveyed by García-Ruiz et al. (2002), being comparable to the amplitude of the largest symmetric warp that they detect, and $> 30\%$ greater than the largest they find in an isolated system. Our estimate of the warp radius ($r_w \sim 33 \text{ kpc}$ on both sides) is indicated by the dashed vertical line in Fig. 11b. There is a slight decrease in θ measured from our I -band photometry from $20 \text{ kpc} < r < 32 \text{ kpc}$, representing a $\sim 1\sigma$ deviation from θ_d . If this is the signature of a warp in the optical disk, then the latter is in the opposite direction from that seen in H I. This disconnect between stellar and H I warps is common in spirals (Briggs 1990, García-Ruiz et al. 2002).

The H I emission within r_w is fairly symmetric about V_{sys} , and there is a good correspondence between $\Sigma_{HI}(r)$ on the approaching and receding sides in Fig. 5d. The peak flux in Fig. 5c and $\int Idv$ in Table A6 are substantially larger than the single-dish estimates obtained from the Arecibo Radio Telescope¹³ (Haynes & Giovanelli 1984; Lewis et al. 1985; Paturel et al. 2003b; though see Bicay & Giovanelli 1986), due to the large angular size of NGC 2862 relative to the Arecibo primary beam at L -band.

The H I RC of NGC 2862 in Fig. 11b extends to $3.5 r_{opt}$ when the warp regions are included, and there is good agreement between the optical and H I kinematics near r_{opt} . There is an asymmetry in the warp region, however, where $V_{obs}(r)$ is $\sim 50 \text{ km s}^{-1}$ lower on the approaching side than on the receding side. We model NGC 2862 using

¹³ The Arecibo Observatory is operated by Cornell University under cooperative agreement with the National Science Foundation.

$V_{obs}(r)$ and $\Sigma_{HI}(r)$, where $\theta = \theta_d$ for $r < r_w$ and θ traces the warp ridge farther out. The simulated datacube recovers the channel map morphology when i_d is adopted for both the main disk and warp emission. We experimented briefly with variations in the warp i , and find that $i < 80^\circ$ in the simulations fails to reproduce the observed warp morphology in the channel maps. The RC flatness in the warp regions and the drop in RC amplitude beyond the warp radius on the approaching side therefore appear to be robust features in the kinematics of NGC 2862.

NGC 2955

NGC 2955 is the lowest i galaxy in the fast rotator sample. Its optical structure is intermediate to a flocculent and a smooth morphology (Elmegreen & Elmegreen 1982), with complete and partial inner rings at $r = 15''$ (7.5 kpc) and $r = 81''$ (41 kpc) as well as a pseudo outer ring at $r = 2.4'$ (73 kpc) (de Vaucouleurs & Buta 1980). None of these features coincides with the “kink” in the I -band surface brightness profiles (Fig. 1) and R -band (Courteau 1996) at $r \sim r_{opt}$ (20 kpc). Both Ramella et al. (1995) and Mahdavi et al. (1999, 2004) assign NGC 2955 to a loose group with 7 – 13 members; none fall within the primary beam and bandwidth of our observations.

The H I emission of NGC 2955 is “clumpy” at all frequencies in Fig. 15e, but overall has the expected morphology of an inclined disk. The H I distribution extends farther on the advancing side of the galaxy than on the receding side (Fig. 6) due to a feature from $6830 - 6787 \text{ km s}^{-1}$. There is a sharp decrease in $\Sigma_{HI}(r)$ beyond r_{opt} on both sides of the disk that coincides with the kink in the surface brightness profile. There are also enhancements in $\Sigma_{HI}(r)$ at the locations of the complete and partial optical inner rings on the approaching side. There is a hint of a warp or other distortion along the minor axis of the velocity field, but the angular resolution along that direction is relatively low (Fig. 6b). The global profile in Fig. 6d is symmetric, and $\int Idv$ is 10–15% larger than previous single dish measurements (Haynes & Giovanelli 1984; Haynes et al. 1999b; Paturel et al. 2003b; Vogt et al. 2004).

The H I RC for NGC 2955 follows the upper envelope of that derived in the optical near r_{opt} (Fig. 12c). The latter varies by $\sim 80 \text{ km s}^{-1}$ in this region, likely due to spiral structure in the disk. There is a systematic decrease of $\sim 2 \text{ km s}^{-1} \text{ kpc}^{-1}$ in $V_{obs}(r)/\sin i_d$ for $r > 27 \text{ kpc}$ of $\sim 2 \text{ km s}^{-1} \text{ kpc}^{-1}$, such that the amplitude of the outermost RC point is $\sim 50 \text{ km s}^{-1}$ lower than the value at r_{opt} . We construct 2 models of the HI emission in NGC 2955 using $V_{obs}(r)$ and $\Sigma_{HI}(r)$: the first adopts i_d and θ_d , and in the second we mimic a warp by gradually decreasing i to 49° to produce a flat RC beyond r_{opt} . We find slightly better agreement between the second simulation and the channel maps in Fig. 15e on the approaching side, but both models recover the receding side of the HI distribution equally well. It is therefore plausible that the turnover beyond r_{opt} in the HI RC in Fig. 12c stems from an under-estimate of i in this region rather than a change in the halo potential.

IC 4202

IC 4202 is an edge-on spiral in the Coma cluster, with a projected separation of 3.82° and radial velocity separation of $\sim 200 \text{ km s}^{-1}$ from the cluster center (Kent & Gunn 1982).

The channel maps of IC 4202 in Fig. 15f show few deviations from the morphology of an edge-on disk. While the outer H I contours from $7361 - 7360 \text{ km s}^{-1}$ and $6906 - 6884 \text{ km s}^{-1}$ bend slightly at large r , there is little evidence for a change in θ in the H I total intensity map of Fig. 7a and we find no conclusive evidence for a warp. As in the single-dish spectrum of Freudling et al. (1988) we find a mild asymmetry in the global profile horns and in $\Sigma_{HI}(r)$. Our estimate of $\int Idv$ is 25% larger than published single-dish values (Giovanelli et al. 1997; Paturel et al. 2003b; Vogt et al. 2004), but there is good agreement between our results and V_{sys} , $W \sin i$ from the literature. A cursory search of the H I datacubes does not reveal any companions.

There is excellent agreement between the optical and H I kinematics in the overlap region, as well as a high degree of symmetry between the approaching and receding sides. However, the H I kinematics do not extend much farther into the halo than the corresponding optical RC (Fig. 11c). We model the IC 4202 datacube using the derived kinematics and $\Sigma_{HI}(r)$, adopting i_d and θ_d from Table 2. At the angular and spectral resolution of our H I data across the disk of IC 4202, these simulations recover the observed frequency dependence of the H I distribution.

NGC 6195

NGC 6195 is an intermediate i spiral in Abell 2199, with a projected separation of 1.61° and radial velocity separation of $\lesssim 100 \text{ km s}^{-1}$ from the cluster center (Zabludoff et al. 1993). A strong $m = 1$ Fourier term in R -band photometry implies a moderate lopsidedness in the stellar disk (Rudnick et al. 2000), and a corresponding increase in disk star formation is inferred from the strength of Balmer absorption and the weakness of the 4000\AA break. The I -band surface brightness distribution in Fig. 1 and the V -band profile of Gavazzi et al. (1994) are also unusual, with a pronounced “dip” for $0.2r_{opt} \lesssim 0.7r_{opt}$ ($3 \text{ kpc} \lesssim r \lesssim 30 \text{ kpc}$): this feature is not a manifestation of extinction in the system given its relatively low i . The shallow FIR spectral index of NGC 6195 between 25 and $60\mu\text{m}$ may indicate AGN activity (Condon et al. 2002).

The H I channel maps for NGC 6195 in Fig. 15g also show some asymmetries, particularly between the SE and NW “wings” of the distribution at 9044 km s^{-1} , 8912 km s^{-1} and 8825 km s^{-1} . The total intensity distribution in Fig. 8a is also lopsided, and the H I extends farther on the approaching side than on the receding side. The 40% difference in the peaks of the global profile in Fig. 8c is less prominent in the single-dish data from Haynes et al. (1997; see also Vogt et al. 2004).

We detect two companions to NGC 6195, $5.7'$ (215 kpc in projection) to the N and $4.0'$ (150 kpc in projection) to the NW of the main disk, respectively. The first is KUG 1634+392, a 16.5^{th} (blue) mag galaxy (Garnier et al.

1996) classified as a UV-excess object by Takase & Miyauchi-Isobe (1984). Its optical dimensions imply a low i : ISM turbulence may therefore be an important contributor to $W \sin i$, and the listed lower limit on M_T is highly uncertain (Table 5). There are no catalogued objects in the vicinity of the NW companion, and it is therefore a new detection. Channel maps (not shown) indicate that the N side is advancing and the S side is receding: this is corroborated by the morphology of a faint counterpart at the same location in our I -band image. Tidal interactions between NGC 6195 and these companions provide a natural explanation for its lopsided stellar disk and enhanced star formation rate.

Despite the unusual stellar and gaseous morphologies of NGC 6195, there is a high degree of symmetry in the hybrid RC (Fig. 12d). The optical kinematics reveal a steep inner rise, and the RC is flat at all measured $r > 2$ kpc. Though our models of the H I channel maps do not reproduce the lopsidedness discussed above, there is broad general agreement between the data and simulations with $V_{obs}(r)$ and $\Sigma_{HI}(r)$ as inputs when i_d and θ_d are adopted throughout the H I disk.

UGC 11455

UGC 11455 is an edge-on field galaxy included in Karachentseva's (1993; see also Karachentsev et al. 1999) Flat Galaxy Catalog. Lüticke et al. (2000a,b) measure an elliptical bulge from surface brightness analyses of NIR and DSS images, and there is no indication of a bar from PV cuts parallel to the major axis in the NIR images.

The channel maps of UGC 11455 in Fig. 15h reveal a warp on the approaching side, most prominent from $5132 - 5090$ km s $^{-1}$. There is also a low column density extension on the receding side from $5667 - 5646$ km s $^{-1}$, though θ is the same as that of the galaxy major axis. We measure a warp angle $\alpha = 12^\circ$ on the approaching side by following the peak of the total intensity distribution Fig. 9a as in García-Ruiz et al. (2002), and the approximate starting location r_w of the warp is indicated by the dashed vertical line in Fig. 11d. The H I distribution is symmetric about the galaxy center beyond the optical disk, and features in $\Sigma_{HI}(r)$ beyond $r \sim 70''$ (26 kpc) are well correlated. There is also good agreement between V_{sys} , $\int Idv$ and $W \sin i$ and single-dish estimates in the literature (Bottinelli et al. 1993; Theureau et al. 1998; Haynes et al. 1999b; Paturel et al. 2003b; Vogt et al. 2004).

We confirm that CGCG 341-027 is a companion to UGC 11455, with a projected separation of $3.4'$ (75 kpc in projection) to the NW and radial velocity separation of 243 km s $^{-1}$ from the latter. CGCG 341-027 is a 15.7^{th} (blue) mag Sb spiral, and our measurement of V_{sys} is in agreement with that of Karachentsev et al. (1985). Channel maps (not shown) indicate that the S side is advancing and the N side is receding, and there is an asymmetry in the global profile with more gas on the receding side in Fig. 9c (though the S/N is low). For comparison, M_{HI} for CGCG 341-027 is half that of the Local Group spiral M33 though its rotational velocity is at least as large as in the latter (Corbelli & Salucci 2000). The presence of a companion to UGC 11455 raises the possibility that the asymmetric HI warp may be tidally driven.

Though the optical RC for UGC 11455 is still rising at the last measured point (Fig. 11), the outer H I RC is flat and extends well beyond r_{opt} on the advancing side. There is good agreement between the two kinematic tracers near the edge of the optical RC on both sides of the disk. We model the H I emission in UGC 11455 using the derived RC and $\Sigma_{HI}(r)$. On the approaching side, we set $\theta = \theta_d$ for $r < r_w$ and vary θ smoothly following the warp angle α farther out; on the receding side, we fix $\theta = \theta_d$ at all r . The simulated datacube recovers the channel map morphology when i_d in Table 2 is adopted for both the main disk and warp emission.

REFERENCES

Bagri, D. S. 1996, Reduction of 1400 MHz RFI in the VLA, VLA Test Memo 200

Begeman, K. G. 1989, A&A, 223, 47

Bicay, M. D., & Giovanelli, R. 1986, AJ, 91, 732

Bosma, A. 1978, Ph.D. thesis, Rijksuniv. Groningen

Bosma, A. 1981a, AJ, 86, 1791

Bosma, A. 1981b, AJ, 86, 1825

Bottinelli, L., Gouguenheim, L., Fouqué, P., & Paturel, G. 1990, A&AS, 82, 391

Bottinelli, L., Durand, N., Fouqué, P., Garnier, R., Gouguenheim, L., Loulergue, M., Paturel, G., Petit, C., & Teerikorpi, P. 1993, A&AS, 102, 57

Braun, R. 1997, ApJ, 484, 637

Briggs, F. H. 1990, ApJ, 352, 15

Broeils, A. H., & Rhee, M.-H. 1997, A&A, 324, 877

Bullock, J. S., Dekel, A., Kolatt, T. S., Kravtsov, A. V., Klypin, A. A., Porciani, C., & Primack, J. R. 2001, ApJ, 555, 240

Burstein, D., & Rubin, V. C. 1985, ApJ, 297, 423

Casertano, S., & van Gorkom, J. H. 1991, AJ, 101, 1231 (CvG91)

Catinella, B., Haynes, M. P., & Giovanelli, R. 2005, AJ, 130, 1037 (C05)

Catinella, B., Giovanelli, R., & Haynes, M. P. 2006, ApJ, in press (astro-ph/0512051)

Christodoulou, D. M., Shlosman, I., & Tohline, J. E. 1995a, ApJ, 443, 551

Christodoulou, D. M., Shlosman, I., & Tohline, J. E. 1995b, ApJ, 443, 563

Clark, B. G. 1980, A&A, 89, 377

Condon, J. J., Cotton, W. D., & Broderick, J. J. 2002, AJ, 124, 675

Corbelli, E., & Salucci, P. 2000, MNRAS, 311, 441

Courteau, S. 1996, ApJS, 103, 363

Courteau, S. 1997, AJ, 114, 2402

Dalcanton, J. J., Spergel, D. N., & Summers, F. J. 1997, ApJ, 482, 659

Dale, D. A., & Giovanelli, R. 2000, ASPC, 201, 25

de Blok, W. J. G., McGaugh, S. S., & van der Hulst, J. M. 1996, MNRAS, 283, 18

de Blok, W. J. G., McGaugh, S. S., Bosma, A., & Rubin, V. C. 2001, ApJ, 552, L23

de Blok, W. J. G., & McGaugh, S. S. 1997, MNRAS, 290, 533

de Blok, W. J. G., Bosma, A., & McGaugh, S. S. 2003, MNRAS, 340, 657

de Jong, R. S. 1996, A&AS, 118, 557

de Jong, R. S., & Lacey, C. 2000, ApJ, 545, 781

de Vaucouleurs, G. 1948, Ann. Astrophys. 11, 247

de Vaucouleurs, G., & Buta, R. 1980, ApJS, 44, 451

de Vaucouleurs, G., de Vaucouleurs, A., Corwin, H. G., Jr., Buta, R. J., Paturel, G., & Fouqué, P. 1991, Third Reference Catalogue of Bright Galaxies (New York: Springer Verlag)

Efstathiou, G., Lake, G., & Negroponte, J. 1982, MNRAS, 199, 1069

Ekers, R. D., & van Gorkom, J. H. 1984, in Indirect Imaging, ed. Roberts, J. A. (New York: Columbia University Press), p. 21

Elmegreen, D. M., & Elmegreen, B. G. 1982, MNRAS, 201, 1021

Freudling, W., Haynes, M. P., & Giovanelli, R. 1988, AJ, 96, 1791

García-Ruiz, I., Sancisi, R., & Kuijken, K. 2002, *A&A*, 394, 769

Garnier, R., Paturel, G., Petit, C., Marthinet, M. C., & Rousseau, J. 1996, *A&AS* 117, 467

Gavazzi, G., Garilli, B., Carrasco, L., Boselli, A., & Cruz-Gonzalez, I. 1994, *A&AS*, 104, 271

Gentile, G., Salucci, P., Klein, U., Vergani, D., & Kalberla, P. 2004, *MNRAS*, 351, 903 (G04)

Gentile, G., Burkert, A., Salucci, P., Klein, U., & Walter, F. 2005, *ApJ*, 634, L145

Giovanelli, R., Haynes, M. P., Rubin, V. C., & Ford, W. K. 1986, *ApJ*, 301, L7

Giovanelli, R., & Haynes, M. P. 2002, *ApJ*, 571, L107

Giovanelli, R., Haynes, M. P., Salzer, J. J., Wegner, G., da Costa, L. N., & Freudling, W. 1994, *AJ*, 107, 2036

— 1995, *AJ*, 110, 1059

Giovanelli, R., Haynes, M. P., Herter, T., Vogt, N. P., Wegner, G., Salzer, J. J., da Costa, L. N., & Freudling, W. 1997, *AJ*, 113, 23

Giuricin, G., Marinoni, C., Ceriani, L., Pisani, A. 2000, *ApJ*, 543, 178

Haynes, M. P., & Giovanelli, R. 1984, *AJ*, 89, 758

Haynes, M. P., Giovanelli, R., Herter, T., Vogt, N. P., Freudling, W., Maia, M. A. G., Salzer, J. J., & Wegner, G. 1997, *AJ*, 113, 1197

Haynes, M. P., Giovanelli, R., Salzer, J. J., Wegner, G., Freudling, W., da Costa, L. N., Herter, T., & Vogt, N. P. 1999a, *AJ*, 117, 1688 (H99)

Haynes, M. P., Giovanelli, R., Chamaraux, P., da Costa, L. N., Freudling, W., Salzer, J. J., & Wegner, G. 1999b, *AJ*, 117, 2039

Honma, M., & Sofue, Y. 1997, *PASJ*, 49, 539

Jing, Y. P., & Suto, Y. 2002, *ApJ*, 574, 538

Kamphuis, J. J. 1993, Ph.D. thesis, Univ. Groningen

Karachentsev, I. D., Karachentseva, V. E., Kudrya, Y. N., Sharina, M. E., & Parnovsky, S. L. 1999, *BSAO*, 47, 5

Karachentsev, I. D., Karachentseva, V. E., Parnovskij, S. L. 1993, *AN*, 314, 97

Karachentsev, I.; Lebedev, V.; Shcherbanovskii, A. 1985, *BICDS*, 29, 87

Karachentseva, V. E. 1973, *SoSAO*, 8, 3

Kent, S. M., & Gunn, J. E. 1982, *AJ*, 87, 945

Koribalski, B. S. et al. 2004, *AJ*, 128, 16

Kregel, M., & van der Kruit, P. C. 2004a, *MNRAS*, 352, 768

Kregel, M., & van der Kruit, P. C. 2004b, *MNRAS*, 352, 787

Kregel, M., van der Kruit, P. C., & Freeman, K. C. 2005, *MNRAS*, 358, 503

Kyazumov, G. A. 1984, *Soviet Astronomy*, 28, 496

Lavezzii, T. E., & Dickey, J. M. 1997, *AJ*, 114, 2437

Lequeux, J. 1983, *A&A*, 125, 394

Lewis, B. M., Helou, G., & Salpeter, E. E. 1985, *ApJS*, 59, 161

Loeb, A., & Peebles, P. J. E. 2003, *ApJ*, 589, 29

Lucy, L. B. 1974, *AJ*, 79, 745

Lüttinger, R., Dettmar, R.-J., & Pohlen, M. 2000a, *A&AS*, 145, 405

— 2000b, *A&A*, 362, 435

Mahdavi, A., Geller, M. J.; Böhringer, H., Kurtz, M. J., & Ramella, M. 1999, *ApJ*, 518, 69

Mahdavi, A., & Geller, M. J. 2004, *ApJ*, 607, 202

Marchesini, D., D'Onghia, E., Chincarini, G., Firmani, C., Conconi, P., Molinari, E., & Zacchei, A. 2002, *ApJ*, 575, 801

Masters, K. L. 2005, Ph.D. Thesis, Cornell University

Mathewson, D. S., Ford, V. L., & Buchhorn, M. 1992, *ApJS*, 81, 413

McGaugh, S. S., Rubin, V. C., & de Blok, W. J. G. 2001, *AJ*, 122, 2381

Mo, H. J., Mao, S., & White, S. D. M. 1998, *MNRAS*, 295, 319

Napier, P. J., Thompson, R. T., & Ekers, R. D. 1983, *Proc. IEEE*, 71, 1295

Noordermeer, E., van der Hulst, J. M., Sancisi, R., Swaters, R. A., & van Albada, T. S. 2005, *A&A*, 442, 137

Ostriker, J. P., & Peebles, P. J. E. 1973, *ApJ*, 186, 4670

Paturel, G., Petit, C., Rousseau, J., & Vauglin, I. 2003a, *A&A*, 405, 1

Paturel, G., Theureau, G., Bottinelli, L., Gouguenheim, L., Coudreau-Durand, N., Hallet, N., & Petit, C. 2003b, *A&A*, 412, 57

Persic, M., & Salucci, P. 1988, *MNRAS*, 234, 131

Persic, M., & Salucci, P. 1990a, *ApJ*, 355, 44

Persic, M., & Salucci, P. 1990b, *ApJ*, 356, 83

Persic, M., & Salucci, P. 1991, *ApJ*, 368, 60

Persic, M., Salucci, P., & Stel, F. 1996, *MNRAS*, 281, 27

Pisano, D. J., Barnes, D. G., Gibson, B. K., Staveley-Smith, L., Freeman, K. C., & Kilborn, V. A. 2004, *ApJ*, 610, 17

Prada, F. et al. 2003, *ApJ*, 598, 260

Ramella, M., Geller, M. J., Huchra, J. P., & Thorstensen, J. R. 1995, *AJ*, 109, 1458

Rhee, G., Valenzuela, O., Klypin, A., Holtzman, J., & Moorthy, B. 2004, *ApJ*, 617, 1059

Roberts, M. S., & Haynes, M. P. 1994, *ARA&A* 32, 115

Roberts, M. S., & Rots, A. H. 1973, *A&A*, 26, 483

Rudnick, G., Rix, H.-W., & Kennicutt, R. C. Jr 2000, *ApJ*, 538, 569

Rupen, M. P. 1999, in *Synthesis Imaging in Radio Astronomy II*, ASP Conf. Ser. 180, ed. Taylor, G. B., Carilli, C. L., & Perley, R. A. (San Francisco: PASP), p. 229

Saglia, R. P., & Sancisi, R. 1988, *A&A*, 203, 28

Sánchez-Saavedra, M. L., Battaner, E., Guijarro, A., López-Corredoira, M., & Castro-Rodríguez, N. 2003, *A&A*, 399, 457

Sancisi, R., & Allen, R. J. 1979, *A&A*, 74, 73

Simon, J. D., Bolatto, A. D., Leroy, A., Blitz, L., & Gates, E. L. 2005, *ApJ*, 621, 757

Sofue, Y., & Rubin, V. C. 2001, *ARA&A*, 39, 137

Spekkens, K., Irwin, J. A. I., & Saikia, D. J. 2004, *MNRAS*, 352, 1145

Spekkens, K. 2005, Ph.D. Thesis, Cornell University

Spekkens, K., Giovanelli, R., & Haynes, M. P. 2005, *AJ*, 129, 2119

Springob, C. M., 2006, Ph.D. Thesis, Cornell University

Springob, C. M., Haynes, M. P., Giovanelli, R., & Kent, B. R. 2005, *ApJS*, 160, 149

Swaters, R. A. 1999, Ph.D. thesis, Rijksuniv. Groningen

Swaters, R. A., Madore, B. F., & Trehewella, M. 2000, *ApJ*, 531, L107

Swaters, R. A., van Albada, T. S., van der Hulst, J. M., & Sancisi, R. 2002, *A&A* 390, 829

Swaters, R. A., Madore, B. F., van den Bosch, F. C., & Balcells, M. 2003, *ApJ*, 583, 732

Takase, B., & Miyachi-Isobe, N. 1984, *AnTok*, 19, 595

Theureau, G., Bottinelli, L., Coudreau-Durand, N., Gouguenheim, L., Hallet, N., Loulergue, M., Paturel, G., & Teerikorpi, P. 1998, *A&AS*, 130, 333

Tully, R. B., & Fouqué, P. 1985, *ApJS*, 58, 67

van den Bosch, F. C., Burkert, A., & Swaters, R. A. 2001, *MNRAS*, 326, 1205

van den Bosch, F. C., & Swaters, R. A. 2001, *MNRAS*, 325, 1017

Vogt, N. P., Haynes, M. P., Herter, T., & Giovanelli, R. 2004, *AJ*, 127, 3273

Valenzuela, O., Rhee, G., Klypin, A., Governato, F., Stinson, G., Quinn, T., & Wadsley, J. 2005, *ApJ*, submitted (astro-ph/05069644)

van Gorkom, J. H. & Ekers, R. D. 1984, in *Synthesis Imaging in Radio Astronomy*, ed. Perley, R. A., Schwab, F. R., & Bridle, A. H. (San Francisco: PASP), p. 341

van Langevelde, H. J., & Cotton, W. D. 1990, *A&A*, 239, L5

Varela, J., Moles, M., Márquez, I., Galletta, G., Masegosa, J., & Bettomi, D. 2004, *A&A*, 420, 873

Warmels, R. H. 1988, *A&AS*, 72, 427

Warner, P. J., Wright, M. C. H., & Baldwin, J. E. 1973, *MNRAS*, 163, 163

Zabludoff, A. I., Geller, M. J., Huchra, J. P., & Ramella, M. 1993, *AJ*, 106, 1301

TABLE A6
H I PROPERTIES OF THE FAST ROTATOR SAMPLE

NGC/IC (1)	$\int I dv$ (Jy km s ⁻¹) (2)	$W \sin i$ (km s ⁻¹) (3)	V_{sys} (km s ⁻¹) (4)	M_{HI} ($10^{10} M_{\odot}$) (5)	r_{HI}/r_{opt} (6)	M_T ($10^{11} M_{\odot}$) (7)	$\log(M_{HI}/M_T)$ (8)	$\log(\sigma_{HI})$ ($M_{\odot} \text{ pc}^{-2}$) (9)	$\log(\sigma_T)$ ($M_{\odot} \text{ pc}^{-2}$) (10)	r_w (kpc) (11)	α ($^{\circ}$) (12)
NGC 1324	10.7 ± 0.3	583 ± 15	5671	1.59 ± 0.05	2.0	7.9 ± 0.4	-1.70 ± 0.03	0.52 ± 0.06	2.22 ± 0.06
UGC 2849	6.3 ± 0.2	506 ± 18	8124	2.01 ± 0.08	2.0	7.1 ± 0.4	-1.55 ± 0.03	0.57 ± 0.06	2.12 ± 0.06
ESO 563G21	27.8 ± 0.5	642 ± 15	4586	3.23 ± 0.06	2.5	14 ± 1	-1.64 ± 0.03	0.45 ± 0.06	2.09 ± 0.07	(36,0)	(6,0)
NGC 2862	15.1 ± 0.3	549 ± 23	4097	1.41 ± 0.03	3.3	8.4 ± 0.4	-1.78 ± 0.02	0.28 ± 0.06	2.06 ± 0.06	(33,33)	(23,19)
NGC 2955	12.8 ± 0.3	441 ± 17	7009	3.33 ± 0.08	2.6	7.7 ± 0.7	-1.36 ± 0.04	0.65 ± 0.06	2.02 ± 0.07
IC 4202	5.2 ± 0.2	511 ± 14	7131	1.32 ± 0.06	2.0	4.7 ± 0.3	-1.55 ± 0.03	0.56 ± 0.07	2.11 ± 0.06	(0,0)	(0,0)
NGC 6195	5.4 ± 0.2	463 ± 16	9004	2.18 ± 0.07	1.8	5 ± 1	-1.36 ± 0.09	0.71 ± 0.06	2.1 ± 0.1
UGC 11455	9.14 ± 0.2	590 ± 17	5389	1.25 ± 0.03	2.0	8.0 ± 0.3	-1.81 ± 0.02	0.33 ± 0.06	2.13 ± 0.06	(19,0)	(12,0)

NOTE. — Col. (2): Integrated line intensity. Col. (3): Velocity width at 50% of the peak, corrected for instrumental broadening. Col. (4): Integrated profile mid-point. Col.(5): H I mass, computed from eq. 2. Col. (6): Ratio of average H I radius to optical radius. Col. (7): Total dynamical mass, computed from eq. 3 (see text). Col. (9): Average H I surface density $\sigma_{HI} = M_{HI}/\pi r_{HI}^2$. Col. (10): Average total surface density $\sigma_T = M_T/\pi r_{HI}^2$. Col. (11): Measured warp radius in highly inclined systems. First number denotes approaching side, second the receding side. We set $r_w = 0$ when no warp is detected. Col. (12): Measured warp angle in highly inclined systems. First number denotes approaching side, second the receding side.